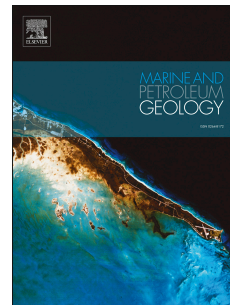


# Journal Pre-proof

How initial basin geometry influences gravity-driven salt tectonics: Insights from laboratory experiments

Frank Zwaan, Matthias Rosenau, Daniele Maestrelli



PII: S0264-8172(21)00298-1

DOI: <https://doi.org/10.1016/j.marpetgeo.2021.105195>

Reference: JMPG 105195

To appear in: *Marine and Petroleum Geology*

Received Date: 15 October 2020

Revised Date: 15 April 2021

Accepted Date: 16 June 2021

Please cite this article as: Zwaan, F., Rosenau, M., Maestrelli, D., How initial basin geometry influences gravity-driven salt tectonics: Insights from laboratory experiments, *Marine and Petroleum Geology* (2021), doi: <https://doi.org/10.1016/j.marpetgeo.2021.105195>.

This is a PDF file of an article that has undergone enhancements after acceptance, such as the addition of a cover page and metadata, and formatting for readability, but it is not yet the definitive version of record. This version will undergo additional copyediting, typesetting and review before it is published in its final form, but we are providing this version to give early visibility of the article. Please note that, during the production process, errors may be discovered which could affect the content, and all legal disclaimers that apply to the journal pertain.

© 2021 Published by Elsevier Ltd.

**CrediT author statement MPG**

**Frank Zwaan:**

Conceptualization, Methodology, Investigation, Writing – Original Draft, Formal Analysis, Validation, Data Curation, Visualization, Project Administration.

**Matthias Rosenau**

Formal Analysis, Data Curation, Visualization, Writing - Review & Editing

**Daniele Maestelli**

Formal Analysis, Data Curation, Visualization, Writing - Review & Editing

**Definitions:**

<https://www.elsevier.com/authors/journal-authors/policies-and-ethics/credit-author-statement>

# How initial basin geometry influences gravity-driven salt tectonics: insights from laboratory experiments

Frank Zwaan<sup>a,b,c\*</sup>, Matthias Rosenau<sup>d</sup>, Daniele Maestrelli<sup>e</sup>

- a) Géosciences Rennes, Unité Mixte de Recherche 6118, CNRS et Université de Rennes 1, Rennes, France
- b) Dipartimento di Scienze della Terra, Università degli Studi di Firenze, Via la Pira 4, 50121 Florence, Italy
- c) Institute of Geological Sciences, University of Bern, Baltzerstrasse 1 + 3, 3012 Bern, Switzerland
- d) Helmholtz Centre Potsdam - GFZ German Research Centre for Geosciences, Telegrafenberg, Potsdam 14473, Germany
- e) Consiglio Nazionale delle Ricerche, Istituto di Geoscienze e Georisorse (CNR-IGG), Via G. La Pira 4, Florence, Italy

\* email: frank.zwaan@geo.unibe.ch

**Keywords:** salt tectonics, margin tilting, salt basin geometry, analogue modelling

## Abstract

As a rifted margin starts to tilt due to thermal subsidence, evaporitic bodies can become unstable, initiating gravity-driven salt tectonics. Our understanding of such processes has greatly benefitted from tectonic modelling efforts, yet a topic that has however gotten limited attention so far is the influence of large-scale salt basin geometry on subsequent salt tectonics. The aim of this work is therefore to systematically test how salt basin geometry (initial salt basin depocenter location, i.e. where salt is thickest, as well as mean salt thickness) influence salt tectonic systems by means of analogue experiments. These experiments were analyzed qualitatively using top view photography, and quantitatively through Particle Image Velocimetry (PIV), and 3D photogrammetry (Structure-from-Motion, SfM) to obtain their surface displacement and topographic evolution. The model results show that the degree of (instantaneous) margin basin tilt, followed by the mean salt thickness are dominant factors controlling deformation, as enhancing basin tilt and/or mean salt thickness promotes deformation. Focusing on experiments with constant basin tilt and mean salt thickness to filter out these dominant factors, we find that the initial salt depocenter location has various effects on the distribution and expression of tectonic domains. Most importantly, a more upslope depocenter leads to increased downslope displacement of material, and more subsidence (localized accommodation space generation) in the upslope domain when compared to a setting involving a depocenter situated farther downslope. A significant factor in these differences is the basal drag associated with locally thinner salt layers. When comparing our results with natural examples, we find a fair correlation expressed in the links between salt depocenter location and post-salt depositional patterns: the subsidence distribution due to the specific salt depocenter location creates accommodation space for subsequent sedimentation. These correlations are applicable when interpreting the early stages of salt tectonics, when sedimentary loading has not become dominant yet.

## 1. Introduction

The deposition of extensive evaporite (salt) deposits is a common occurrence during and after continental break-up and the associated marine transgressions. Examples of such evaporite deposits are found at numerous passive margins around the world (e.g. Hudec & Jackson 2006, 2012; Brun & Fort 2011; Tari & Jabour 2013; Rowan 2014, 2018; Warren 2016, Jackson & Hudec 2017), whereas rift-related deposition of evaporites is on-going in the Afar rift in East Africa (Bonatti et al. 1971). As the margin starts tilting due to thermal subsidence of the adjacent oceanic basin (Fig. 1b), sufficiently large evaporitic bodies can become gravitationally unstable, initiating gravity gliding-type salt tectonics in which post-salt sediments are detached from the pre-salt substratum and transported downslope (e.g. at the Angolan and Brazilian margins of the South Atlantic, Marton et al. 2000; Fort et al. 2004a; Quirk et al. 2012; Jackson et al. 2015). Typical of such salt tectonic systems is the development of upslope extensional structures including rotated blocks and rollovers, a mid-slope translational domain and a downslope compressional domain with diapirs, folding and faulting (e.g. Demercian et al. 1993; Spathopolous 1996; Rowan et al. 2004; Brun & Fort 2011, Fig. 1c). In some cases, the evaporites can even pierce the sedimentary cover and extrude downslope over the exposed seafloor (e.g. Rowan et al. 2004; Hudec & Jackson 2006; Tari & Jabour 2013). Within this context, it must be stressed that next to margin tilt, sedimentary loading can have an important influence on the development of salt tectonic systems and the relative significance of both driving forces remains debated (e.g. Schultz-Ela 2001; Brun & Fort 2011, 2012; Rowan et al. 2012; Goteti et al. 2013; Peel 2014; Warren 2016),

Evaporite units and associated salt tectonic structures are notoriously challenging to interpret and reconstruct on seismic lines, and our understanding of salt tectonic processes has greatly benefitted from analogue and numerical modelling efforts (e.g. Cobbold & Szatmari, 1991; Gaullier et al., 1993; Vendeville et al. 1995; Mauduit & Brun 1998; Fort et al. 2004a, Gemmer et al. 2004; Ings et al., 2004; Gaullier and Vendeville, 2005; Peel 2014; Brun & Fort 2004, 2011; Quirk et al. 2012; Goteti et al. 2013; Allen & Baumont 2012, 2015; Ferrer et al. 2017; Ge et al. 2019a,b; Pichel et al. 2018; 2019). Such studies provided insights into the structural evolution of the various domains within gravity gliding systems, for instance showing how deformation may migrate up- and downslope over time (Fort et al. 2004a, Brun & Fort 2004, 2011; Quirk et al. 2012; Ge et al. 2019a, b). Also the interaction between (syn-kinematic) sedimentation and salt tectonics has received much attention. Fort et al. (2004b) for instance demonstrated how differential sedimentation along a margin can cause downslope velocity differences resulting in block rotation about a vertical axis. Recently, Goteti et al (2013) and Ge et al. (2019a) have experimented with varying sedimentation patterns, finding that differential sedimentation may lead to the widespread formation of minibasins, thus preventing the development of a well-defined translational domain. Next to the influence of sedimentation, the effects of different margin inclination histories (i.e. instant, vs. progressive) have been investigated as well, showing that faster margin tilting enhances (initial) downward displacement (e.g. Goteti et al. 2013) and causes more distributed deformation (Ge et al., 2019b).

A factor that has however gotten only limited attention until recently is the effect of salt layer thickness variations due to different basin geometries during initial salt deposition. Such variations may be due to the characteristics of the margin; a wide rifted margin would allow for extensive salt deposits, whereas a narrow margin provides only limited space. Also the thermal profile of the lithosphere may influence salt deposition patterns, given that salt is often accumulated during the later stages of continental break-up and the onset of thermal sag (e.g. Rowan 2018, and references therein). Another process affecting these systems is pre-salt sedimentation, which may smoothen the base of the salt basin by covering the otherwise rough bathymetry created by syn-rift faulting (e.g. Strozyk et al. 2017, Fig 1d). However, when syn-rift salt deposition occurs, active faulting may cause the development of smaller and isolated salt basins with limited potential for salt-tectonic deformation (Brun & Fort 2008, 2011; Tari & Jabour 2013; Rowan 2014, Jackson & Hudec 2017).

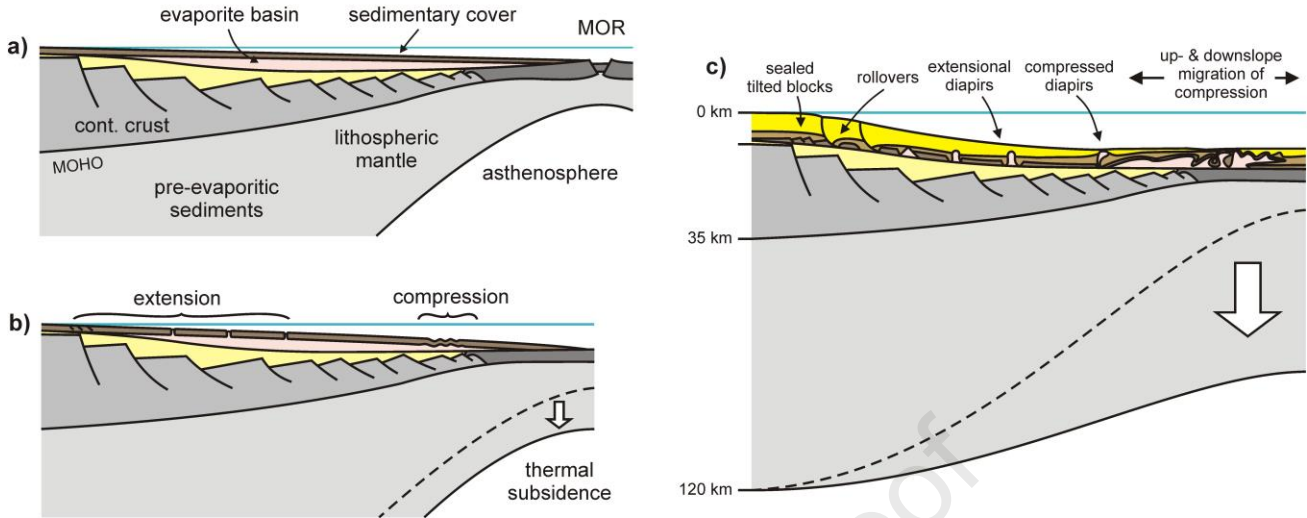
103 Salt basins can thus exhibit a high degree of geometric variability (e.g. Peel et al. 1995; Gamboa et  
104 al. 2008; Marton et al. 2000, PFA 2011; Zalán et al. 2011; Davison et al. 2012; Guerra & Underhill  
105 2012; Garcia et al. 2012; Tari & Jabour 2013; Strozyk et al. 2017, Fig. 1d and e), and such  
106 variations, which can also occur along the length of an evolving rift system or passive margin (e.g.  
107 McClay et al. 2002; Zwaan et al. 2016, Deptuck & Kendell 2017; Rowan 2018), have important  
108 effects on subsequent salt tectonic deformation.

109  
110 While earlier salt tectonic modelling studies have often involved a viscous layer with a constant  
111 thickness (e.g. Cobbold et al. 1989; Mauduit et al. 1997; Mauduit & Brun 1998), more recent  
112 modelling efforts have started to explore the effects of initial salt basin geometries on salt tectonics.  
113 Fort et al. (2004a, b) pioneered the effects of more realistic salt basins with salt pinching out  
114 towards both the upslope and downslope ends of the basin, whereas other researchers have  
115 studied the effects base-salt relief at various wavelengths. For instance, Gaullier et al. (1993),  
116 Maillard et al. (2003), Adam & Krezsek (2012), Dooley & Hudec (2017), Dooley et al. (2017, 2018),  
117 Ferrer et al. (2017) and Pichel et al. (2018, 2019) describe the influence of single or multiple  
118 (oblique) basement steps or sub-salt seamounts and ridges on salt tectonic systems. Depending  
119 whether they represent a thinning or a thickening of the salt layer, such short wave length steps and  
120 obstacles within a salt basins can either accelerate or decelerate salt flow through basal drag  
121 (Dooley et al. 2017). If sufficiently reducing salt thicknesses, base-salt relief may divide the system  
122 in different segments behaving as separate salt basins, with contractional structures upslope and  
123 (enhanced) extensional structures downslope of the relief (e.g. Dooley et al. 2017; Ferrer et al.  
124 2017; Jackson and Hudec 2017). The specific arrangement of such base-salt relief can lead to  
125 highly complex deformation structures, with important variations both along and across a margin  
126 (e.g. Dooley & Hudec 2017; Dooley et al. 2018).

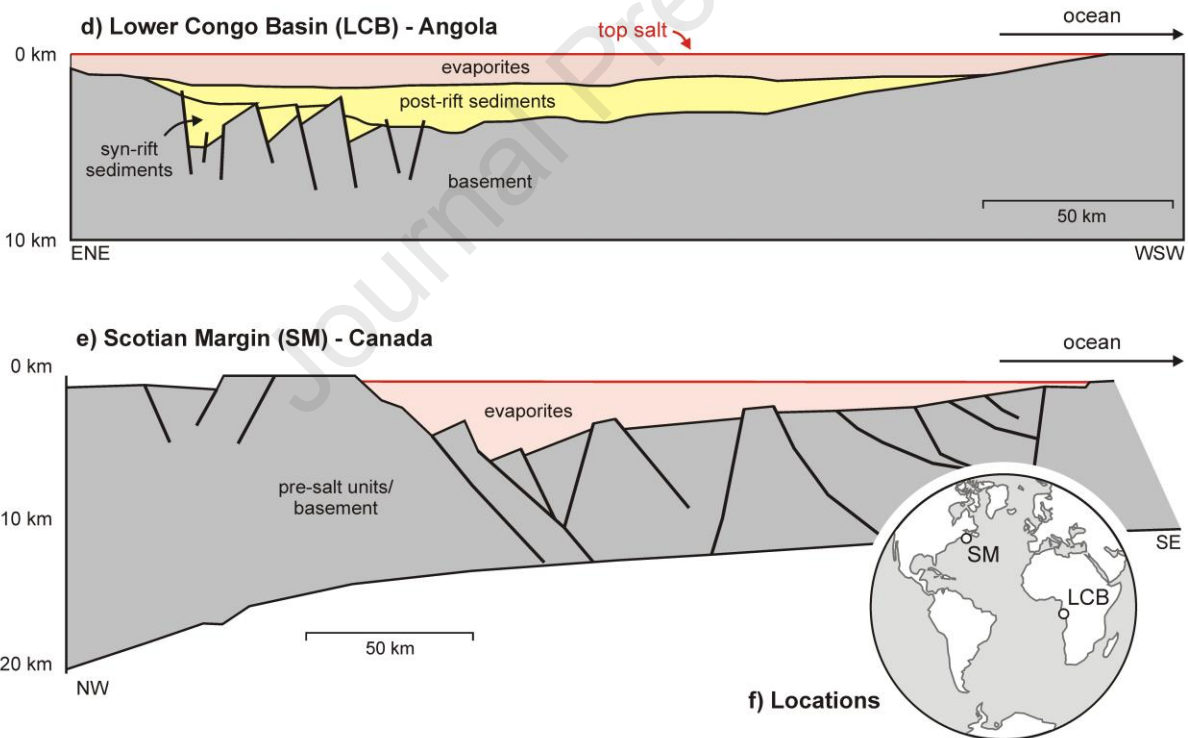
127  
128 Yet these modelling studies generally aim to simulate specific (features of) salt basins and the  
129 resulting salt tectonic deformation, and although some studies have included various salt basin  
130 shapes, these are somewhat limited in their scope since they either aim to mimic specific natural  
131 examples (e.g. Adam & Krezsek 2012) or remain rather conceptual, involving artificial geometries  
132 (e.g. Albertz & Beaumont 2010). We thus conclude that the effect of long wave length salt basin  
133 geometry, specifically initial salt depocenter location, on salt tectonics remains to be explored more  
134 systematically, providing an incentive for further research. In this paper we therefore build on  
135 previous work exploring the effects of basin geometry on salt tectonics by systematically testing the  
136 influence of (1) initial salt basin depocenter location and (2) mean salt thickness on salt tectonic  
137 systems through simple brittle-viscous (and viscous-only) analogue experiments.

138

### evolution of a salt-containing passive margin



### initial salt basin shapes (undeformed salt)



139  
140  
141  
142  
143  
144  
145  
146  
147

**Fig. 1.** (a-c) Generalized tectonic evolution of a passive margin containing evaporite deposits undergoing differential thermal subsidence and oceanward tilting. Image modified after Fort et al. (2004a) and reproduced with permission from the AAPG. (d-g) Reconstructions of undeformed evaporite basins in presently tilted passive margins within the Atlantic realm. (d) Lower Congo Basin, offshore Angola, with an evaporite depocenter downslope (i.e. towards the ocean). Image modified after Marton et al. (2000). (e) Section NS 2000 across the Scotian Margin, offshore eastern Canada, with a main evaporite basin depocenter upslope. Image modified after PFA (2011). (f)

148 *Locations of natural examples (d-g). LCB: Lower Congo Basin, MOHO: Mohorovičić discontinuity,*  
149 *MOR: mid-oceanic ridge, SM: Scotian Margin.*

Journal Pre-proof



150 **2. Experimental methods**151  
152 **2.1. Model Materials**

153  
154 Our analogue models involved a brittle-viscous model configuration, which is routinely used for salt  
155 tectonic modelling studies (e.g. Cobbold & Szatmari, 1991; Gaullier et al., 1993; Mauduit & Brun  
156 1998; Fort et al. 2004a, Brun & Fort 2011; Gaullier and Vendeville, 2005; Ge et al. 2019a, b). To  
157 represent a basal salt layer in a salt tectonic system we applied a locally up to 10 mm thick body of  
158 transparent silicone (polydimethylsiloxane or PDMS, type SGM-36 produced by Dow Corning with a  
159 density ( $\rho$ ) of ca. 965 kg/m<sup>3</sup> and viscosity ( $\eta$ ) of ca.  $3 \cdot 10^4$  Pa·s Weijermars 1986; Rudolf et al.  
160 2016; Zwaan et al. 2018). This viscous material has a Newtonian rheology ( $n = \text{ca. } 1$ ) under  
161 standard experimental conditions, which makes it very suitable for modeling salt flow (e.g. Fort et al.  
162 2004a, b). A 0.6 cm thick layer of fine-grained Fine ( $\phi = 200\text{-}300 \mu\text{m}$ ), homogeneous sorted and  
163 well-rounded Fontainebleau quartz sand was used to represent brittle post-salt (suprasalt)  
164 sedimentary cover. This sand has an internal friction coefficient of ca. 0.6 and negligible cohesion  
165 (Vendeville et al. 1987; Fort et al. 2004a), making it a suitable analogue for modelling brittle  
166 materials in nature. The sand is sieved onto the PDMS layer below in order to ensure a constant  
167 density ( $\rho$ ) of ca. 1400 kg/m<sup>3</sup>. Note that the resulting density contrast between salt and sediment  
168 layers in the models is slightly exaggerated. Material characteristics are summarized in Table 1.

169  
170 *Table 1. Material properties*  
171

<b>Granular material: Fontainebleau quartz sand<sup>a</sup></b>	
Grain size range	200-300 $\mu\text{m}$
Density (sieved) ( $\rho$ )	1400 kg/m <sup>3</sup>
Angle of internal friction ( $\phi$ )	30-33°
Coefficient of internal friction ( $\mu$ )	0.58-0.65
Cohesion (C)	negligible
<b>Viscous material: SGM-36 PDMS<sup>b</sup></b>	
Density ( $\rho$ )	965 kg/m <sup>3</sup>
Viscosity <sup>c</sup> ( $\eta$ )	ca. $2.8 \cdot 10^4$ Pa·s
Rheology	Newtonian ( $n \sim 1$ ) <sup>d</sup>

172  
173 <sup>a</sup> Quartz sand characteristics after Vendeville et al. (1987) and Fort et al. (2004a)

174 <sup>b</sup> Pure PDMS rheology after Rudolf et al. (2016)

175 <sup>c</sup> Viscosity value holds for model strain rates  $< 10^{-2} \text{ s}^{-1}$

176 <sup>d</sup> Power-law exponent  $n$  (dimensionless) represents sensitivity to strain rate and holds for model strain rates  $< 10^{-2} \text{ s}^{-1}$

177

178

179



## 180 2.2. Model set-up

181

182 For this study we tested a total of ten salt basin geometries (Fig. 2). These ten basin geometries can  
183 be subdivided in two sets of five geometries each (Fig. 2). The first set (basin shapes 1-5) consisted  
184 of salt basins with a single 10 mm deep depocenter (3 km in nature) that all have the same mean  
185 salt basin depth (5 mm, i.e. 1.5 km in nature) (Fig. 2a). The use of this general single-depocenter  
186 geometry for salt tectonic modelling was first introduced by Fort et al. (2004a, b) based on the initial  
187 salt distribution in post-rift evaporite basins along the Angolan margin (e.g. the Lower Congo Basin,  
188 Fig. 2d) and has been used routinely by other studies since (e.g. Ge et al. 2019a, b). We  
189 systematically varied the location of the salt depocenter between the basins (defined by distance  $D$ ,  
190 measured from the upslope edge of the basin). From basin to basin, the salt depocenter location  
191 was shifted upslope to simulate different basin shape (e.g. the Scotian Margin, Fig. 2f). As a result,  
192 also the basin floor inclination and the change in salt thickness as a function of the distance from  
193 the model salt depocenter on both sides varied from model to model. The first basin in this set  
194 (basin shape 1) represented the extreme endmember of a halfgraben structure filled with syn-rift salt  
195 and with the abrupt downslope buttress representing a steep boundary fault (Fig. 2a).

196

197 The second set of model salt basin geometries (basins shapes 6-10) involved basin geometries with  
198 a central flat part of the basin floor (Fig. 2b). These were used to represent basins with varying  
199 mean salt isopachs, either by varying the extent of the flat basin floor and/or reducing the maximum  
200 thickness of the salt layer from the regular 10 mm to 5 mm (basin shapes 9 and 10, Fig. 2a, b). The  
201 gentle basin floor would be typical of post-rift salt basins, but similar to basin shape 1, the steep  
202 downslope end of basin shape 6 would imply syn-rift salt deposition in a halfgraben-like structure  
203 with a boundary fault at the downslope basin end (Fig. 2b). Alternatively, the steep downdip salt  
204 barrier could represent a volcanic high as observed in the Kwanza and Santos Basins on opposite  
205 sides of the South Atlantic (Quirk et al. 2012).

206

207 All model salt basins were 60 cm long (x-axis) and 40 cm wide (y-axis), translating to 180 x 120 km  
208 in nature. They were made out of parts of PVC (for the basin floor) and wood (for the vertical  
209 upslope and side edges of the models) (Fig. 2c). These parts were fully covered with regular duct  
210 tape to seal any slits between them and to ensure homogeneous boundary conditions in all models.  
211 The basins were filled with the PDMS silicone oil representing the model salt layer, on top of which  
212 the 6 mm thick suprasalt cover of homogeneous Fontainebleau sand was added. This sand cover  
213 which extended for ca. 10 cm beyond the salt basin's downslope end (Fig. 2). After model  
214 preparation, the models were instantaneously tilted by either 1 or 3 degrees, to simulate the  
215 marginal inclination due to differential thermal subsidence (Fig. 1a-c). Following this initial tilting, the  
216 models were left to evolve for two days (48h). No syn-tectonic sedimentation was applied.

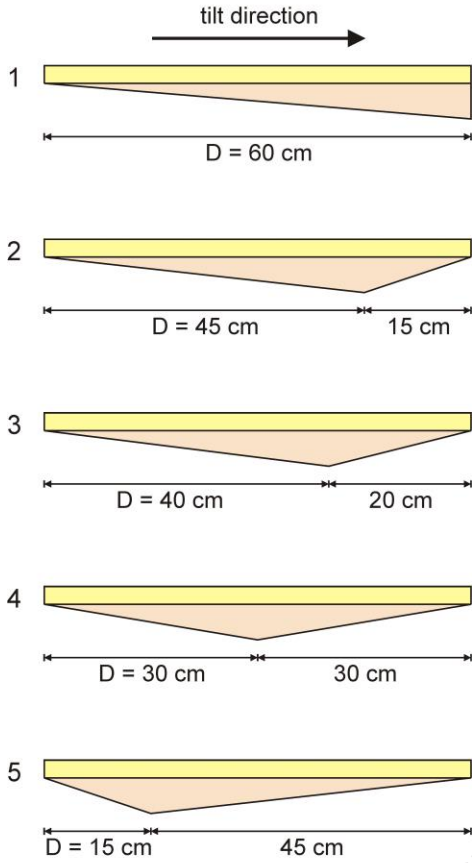
217

218 We completed a total of 35 experiments, including reruns (Table 2) that are divided in three series.  
219 The first series (Series I) contains all experiments simulating a 1° margin tilt (Models A-J). The  
220 second series (Series II) contains experiments with a 3° margin tilt (Models K-W, where the Models  
221 U-W were reruns of Models P-T, the results of which are provided in the supplementary material,  
222 Zwaan et al. 2021). As a reference, we also completed a third series (Series III) involving models  
223 without a sand cover in which we aimed to reproduce the response of a purely viscous system. The  
224 total lack of a suprasalt sediment cover is likely unrealistic, hence the results of these models are  
225 not part of the main text and are shown in the Appendix only.

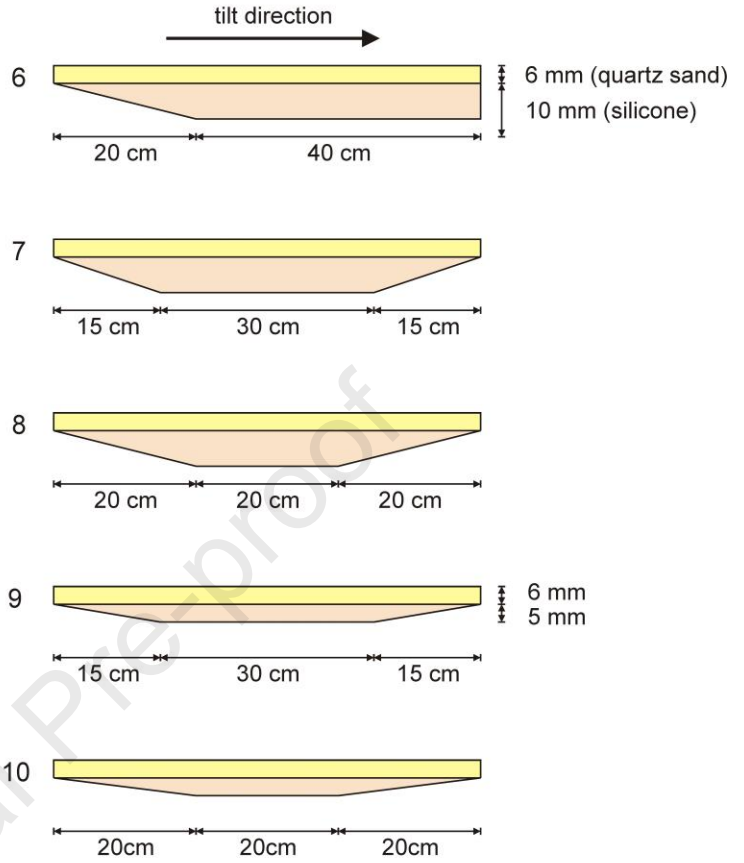
226

227

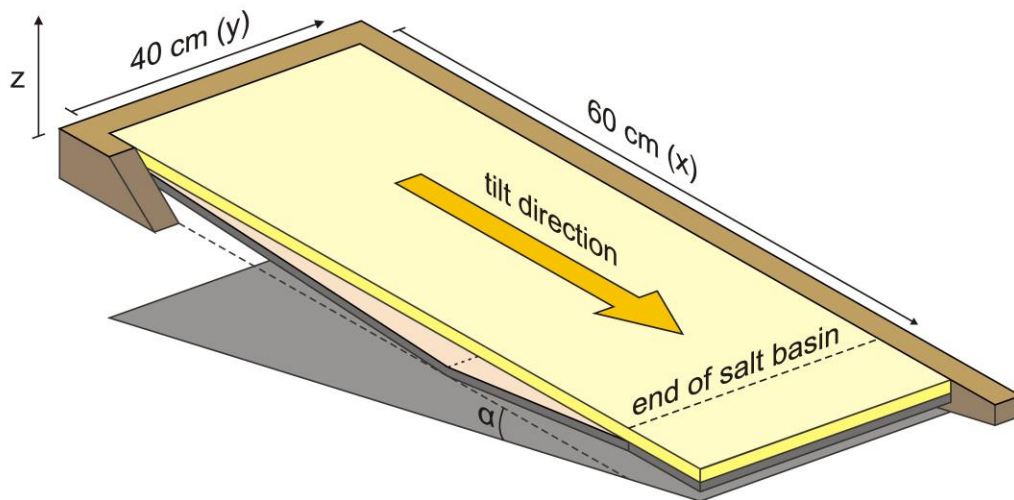
a) basin geometries simulating a single salt basin decenter



b) basin geometries simulating a partially flat salt basin floor



c) 3D sketch of model run



228  
229  
230

231 **Fig. 2.** Model set-up. (a) Salt basin geometries 1-5 with a single depocenter, where the maximum  
 232 model salt thickness is 10 mm. Note that  $D$  is defined as the distance between the upslope edge of  
 233 the model salt basin and the basin depocenter. (b) Basin geometries involving a partially flat basin  
 234 floor 6-10, with a maximum model salt layer thickness of 5 mm for basin geometries 9 and 10,  
 235 instead of the standard 10 mm. (c) 3D Sketch of model run, during which the basin is tilted by either  
 236  $1^\circ$  or  $3^\circ$  (angle  $\alpha$ ) towards the positive  $x$ -direction. These sketches represent models from Series I  
 237 and II (experiments with a brittle cover), but the same salt basin shapes without sand cover were  
 238 applied for Series III (see Appendix A1 for results from this model series). Model details are listed in  
 239 Table 2.

240

241

242

243 **Table 2. Model details.**

244

			<b>Series I</b> (0.6 mm brittle cover, $1^\circ$ basin tilt)	<b>Series II</b> (0.6 mm brittle cover, $3^\circ$ basin tilt)	<b>Series III</b> (no brittle cover, $3^\circ$ basin tilt) <sup>§</sup>
<b>Basin Geometry*</b>	<b>Depocenter location (distance <math>D</math>)</b>	<b>Mean silicone (model salt) layer thickness</b>	<b>Model name</b>	<b>Model name</b>	<b>Model name</b>
1	60 cm	5.0 mm	A	K	Z1 <sup>†</sup>
2	45 cm	5.0 mm	B	L	Z2 <sup>†</sup>
3	40 cm	5.0 mm	C	M	Z3 <sup>†</sup>
4	30 cm	5.0 mm	D	N	Z4 <sup>†</sup>
5	15 cm	5.0 mm	E	O	Z5 <sup>†</sup>
6	-	8.3 mm	F	U ( $P^\#$ )	Z6
7	-	7.5 mm	G	V ( $Q^\#$ )	Z7
8	-	6.7 mm	H	W ( $R^\#$ )	Z8
9	-	3.8 mm	I	X ( $S^\#$ )	Z9
10	-	3.3 mm	J	Y ( $T^\#$ )	Z10

245

246 \* see Fig. 2 for basin geometry description

247 # test runs of models U-Y without stereographic photos, not discussed in this paper. For  
248 results see the supplementary materials (Zwaan et al. 2021).

249 \$ Series III models are presented in Appendix A1 only

250 † model ran for 49 h instead of 48 h

251

252

253

254

### 2.3. Analogue model scaling

Analogue models scale down from nature in terms of geometry, kinematics and dynamics (e.g. Hubbert, 1937; Ramberg, 1981). Based on dimensionless numbers representing ratios of forces, scaling factors for the basic dimensions of length, mass and time are derived. Here we use the ratio between lithostatic pressure and viscous strength (the so-called Ramberg number  $R_m$ )

$$R_m = \rho g h^2 / \eta v \quad (1)$$

where  $\rho$  represents density,  $g$  the gravitational acceleration,  $h$  height,  $\eta$  dynamic viscosity and  $v$  velocity, to scale the viscous regime (e.g. Ramberg 1981; Adam & Krezsek, 2012; Gemmer et al., 2005). In the brittle regime, the friction coefficient  $\mu$  defining the depth dependency of frictional strength, is used as a dimensionless parameter for cohesionless materials. By keeping  $\mu$  and  $R_m$  similar in the model and in nature (ca. 0.6, Table 3) scaling factors for all relevant dimensions and parameters can be derived. From equations (1), it follows that the time scale ratio ( $t^*$ ) depends directly on the initial choice of length scale, density and viscosity for experiments conducted under normal gravity (convention:  $\rho^* = \rho_{\text{model}} / \rho_{\text{nature}}$ ):

$$t^* = \rho^* g^* h^* / \eta^* \quad (2)$$

In this study, the geometric scaling or height ratio ( $h^*$ ) is  $3.3 \cdot 10^{-6}$  (1 cm in the model is 3 km in nature). The time scaling ( $t^*$ ) is subsequently dictated by the effective density (i.e. reduced by the water density for submarine systems by a factor of c. 1/2) and the ratio between the viscosity of natural salt versus silicone oil at typical model strain rates, is in the order of  $5 \cdot 10^{-16}$  (Table 3). Therefore, 1 hour in the model translates to approximately 0.6 Myr in nature and the standard model duration of 48 h represents 29 Myr of basin evolution. We note that while the friction coefficient of our brittle cover analogue is similar to nature (ca. 0.6), the density ratio between the brittle viscous materials in our models is somewhat higher than in nature (1.45 in our models vs. 1.05 in nature). This results in buoyancy forces which are slightly exaggerated but considered not problematic in our experiments.

Furthermore, the models should have similar proportions as their natural prototype. Salt basins in nature are usually some hundreds of kilometres large ( $L$ ) and a few kilometres deep ( $h$ ), giving an  $L/h$  ratio of  $10^2$ - $10^3$  (e.g. Brun & Fort, 2011; Strozzyk et al. 2017). The salt basin analogues in this study are 60 cm long (measured across-margin) and the simulated salt layers are 0.5 to 1 cm deep at the deepest point (translating to 180 km and 1.5-3 km, respectively). These dimensions yield an  $L/h$  ratio ranging from 60 to the order of  $10^2$ , which we deem sufficiently close to the natural values to state that our models are adequately scaled. An overview of scaling parameters is provided in Table 3.

**Table 3. Scaling parameters**

	General parameters		Brittle sediments		Ductile evaporites		Dynamic scaling	
	Gravitational acceleration $g$ (m/s <sup>2</sup> )	Height $h$ (m)	Density $\rho$ (kg/m <sup>3</sup> )	Friction coefficient $\mu$	Density $\rho$ (kg/m <sup>3</sup> )	Viscosity $\eta$ (Pa·s)*	Velocity $v$ (m/s)	Ramberg number $R_m$
Model	9.81	0.01	1400	0.6	965	$2.8 \cdot 10^4$	$5.8 \cdot 10^{-7}$	58
Nature	9.81	3000	2300	0.6	2200	$5 \cdot 10^{19}$	$7.9 \cdot 10^{-11}$	49
Ratios	1	$3.3 \cdot 10^{-6}$	0.61	1	0.44	$5.6 \cdot 10^{-16}$	$7.3 \cdot 10^4$	1.2

\* Natural salt viscosities may vary significantly (between  $10^{14}$  and  $10^{20}$  Pa·s, Jackson and Talbot 1986, and references therein).

299  
300  
301  
302  
303  
304  
305  
306  
307  
308  
309  
310  
311  
312  
313  
314  
315  
316  
317  
318  
319  
320  
321  
322  
323  
324  
325  
326  
327  
328  
329  
330  
331  
332  
333  
334  
335  
336  
337  
338  
339  
340  
341  
342  
343  
344  
345  
346  
347  
348  
349  
350

## 2.4. Analogue model analysis

All models were monitored by means of top view topography; digital images of the models were taken every 15 min (12 minutes for some) for the duration of the model run using customer grade 10 megapixel cameras. A grid of equidistant dots with laterally reduced spacing (5 cm vs. 2.5 cm near the long ends and downslope end of the model salt basins), made of black dyed sand, was applied on the model surface which allows a visual appreciation of surface deformation.

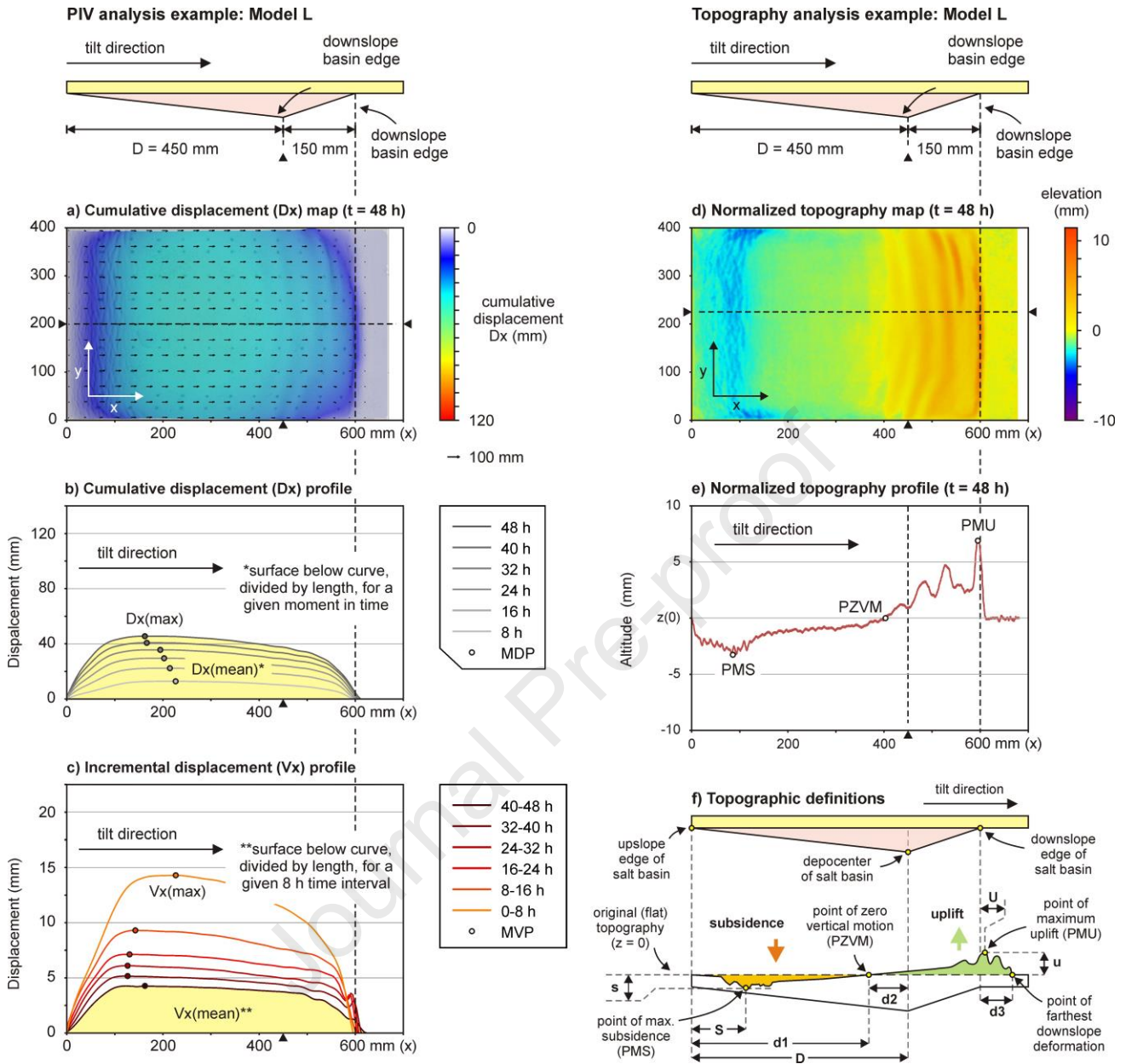
Furthermore, by sieving fine coffee powder on top of the model surface we created a random pixel pattern for digital image correlation (DIC) analysis. Particle Image Velocimetry methods (PIV, e.g. Adam et al., 2005, Boutelier et al. 2019 and references therein) allowed for quantification of 2D horizontal surface displacement monitoring at high precision ( $<0.1$  pixel). We used commercial LaVision Davis 8 software applying 2D-DIC processing through a least squares method with subset and step sizes of 59 and 10 pixels, respectively. With an effective image resolution of c. 0.5 mm per pixel, incremental displacements were derived with a precision of c. 50 microns. The resolution of the displacement field (grid point spacing) defined by the step size is about 5 mm.

PIV analysis yields incremental downslope displacement (or velocity,  $V_x$ ) and cumulative downslope displacement ( $D_x$ ) data accumulated over the duration of a model run. These data are documented in maps of finite surface displacement showing total displacement accumulated over a model run, as well as in profiles extracted along the central axis of each model over 6 intervals of 8 hours each (Fig. 3). These profiles illustrate the evolution of surface displacement, where  $D_x$ -plots provide the cumulative model development, while  $V_x$ -plots visualize displacement variations over time. Note that in principle,  $D_x$  is the sum of  $V_x$ . The plots also provide the location and amount of maximum incremental and cumulative displacements for each time interval (i.e.  $V_{x_{max}}$  measured at the maximum velocity point [MVP] and  $D_{x_{max}}$  at the maximum displacement point [MDP], respectively), Fig. 3). Besides the  $V_{x_{max}}$  and  $D_{x_{max}}$  values that represent strictly point values, we also derived the mean displacement over time (i.e.  $V_{x_{mean}}$  and  $D_{x_{mean}}$ , by taking the area below the relevant curve, divided by the curve's length) as a proxy for model wide deformation (Fig. 3b, c).

In addition, we also took photographs of our experiments from different perspectives at the start and end of each model run. These images allow reconstruction of the model surface with the use of photogrammetry software (Agisoft Photoscan), based on the Structure-from-Motion method (SfM), and is used here to analyze the vertical component of model deformation not captured by 2D PIV analysis. The digital elevation models (DEM) of the start and end of each model run were used to create normalized topography maps with an error below  $\pm 0.5$  mm. We also extracted normalized final topographic profiles along about the same central axis of the model we used for the PIV profiles, complementing the horizontal displacement results derived by PIV analysis (Fig. 3).

We subsequently analyzed a total of eight individual morphometric parameters on the normalized final topographic profiles, of which the definitions are as follows. Total mass displacement is the area of the subsided part of the profile that equals the uplifted part of the profile (shown in orange and green in Fig. 3f, respectively). The maximum subsidence ( $s$ ) is measured at the point of maximum subsidence (PMS), i.e. the deepest part of the depression in the upslope extensional domain. The location of the PMS is defined by distance  $S$ , calculated from the upslope salt basin end. Vice versa, the maximum uplift ( $u$ ) is measured at the point of maximum uplift (PMU), i.e. the highest point in the downslope compressional domain, the location of which is defined as distance  $U$ . Distance  $d_1$  is the distance between the point of (final) zero vertical motion (PZVM, i.e. where the profile cuts the altitude  $[z] = 0$  line) and the salt basin upslope end, whereas distance  $d_2$  is the distance between the PZVM and the basin depocenter. Distance  $d_3$  is the distance between the farthest downslope limit of deformation and the downslope edge of the salt basin.





351  
352  
353  
354  
355  
356  
357  
358  
359  
360  
361  
362  
363  
364  
365  
366  
367

**Fig. 3.** Definitions used for PIV analysis and topography analysis (example: Model L with decenter location at distance  $D = 450$  mm from the upslope salt basin end). (a) Final cumulative displacement ( $D_x$ ) presented in map view ( $t = 48$  h). (b) Cumulative downslope displacement ( $D_x$ ) evolution plotted along a central profile indicated in (a). MDP: maximum displacement point, where  $D_x$  is highest at specific moment in time:  $D_x(\max)$ .  $D_x(\text{mean})$  is the mean cumulative displacement over a specific time interval, calculated by dividing the surface below the  $D_y$  curve by its length. (c) Incremental downslope displacement (i.e. displacement velocity,  $V_x$ ) evolution along a central profile indicated in (a). MVP: maximum velocity point, where  $V_x$  is highest for a specific time interval:  $V_x(\max)$ .  $V_x(\text{mean})$  is the mean displacement over a specific time interval, calculated by dividing the surface below the  $V_y$  curve by its length. (d) Normalized final topography presented in map view. (e) Normalized final topography presented along a profile indicated in (d). PMS: point of maximum subsidence, PMU: point of maximum uplift, and PZVM: point of (final) zero vertical motion, i.e. the intersection of the topography with zero altitude. (f) Topographic parameters.  $D$ : distance between decenter and upslope salt basin end,  $d_1$ : distance between upslope end of basin and PZVM,  $d_2$ :

368 *distance between depocenter and PZVM,  $d_3$ : distance between downslope end of basin and point*  
369 *of farthest downslope deformation,  $S/s$ : location and amount of maximum vertical subsidence in the*  
370 *upslope extensional domain,  $U/u$ : location and amount maximum uplift in the downslope*  
371 *contractional domain. The colored surfaces below and above the topography curve (orange and*  
372 *green, respectively) are of equal size, each indicating the displaced mass along the profile.*  
373  
374  
375  
376  
377

### 378 **3. Results**

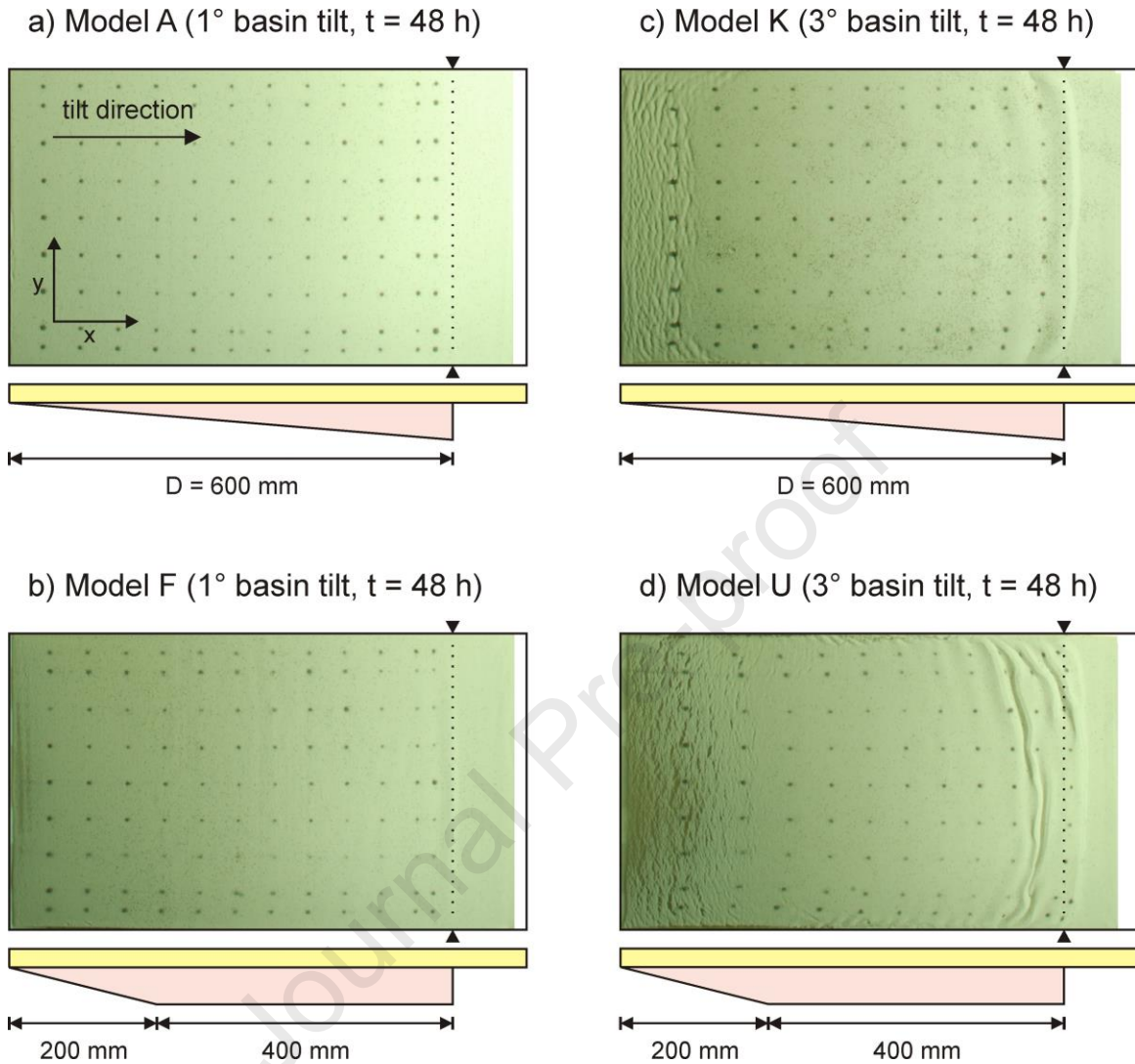
#### 379 **3.1. Qualitative observations from plan view visual inspection**

381 We present a snapshot of final model surface structures in Fig. 4, highlighting some of the general  
382 characteristics of our experiments. Models with  $1^\circ$  basin tilt (Models A and F from series I, Fig. 4a,  
384 b) generally showed, apart from a slight downslope displacement of the surface grid, almost no  
385 visible deformation in the sand layer. Only some minor folding occurred at the downslope basin  
386 edge in Model F (which had the highest mean salt thickness in Series I, see Table 1) accompanied  
387 by slight extensional faulting at the upslope end.  
388

389 By contrast, experiments with  $3^\circ$  basin tilt (Models K and U from series II, Fig. 4c, d) developed clear  
390 extensional structures in their upslope domain, as well as contractional structures at the downslope  
391 margin of the model salt basin with a zone of translational displacement in between. The  
392 contractional structures even migrated beyond the downslope end of the model salt basin, forming a  
393 salt-cored overthrust. These structures are more pronounced in Model U, which has the highest  
394 mean salt thickness. In these  $3^\circ$  basin tilt experiments we also observed a curving of structures  
395 along the long edges of the model (concave downslope orientations for extensional features and  
396 convex upslope curving folds and thrusts in the compressional domain) reflecting the effect of lateral  
397 drag due to boundary friction there (e.g. Fort et al. 2004b, Ge et al. 2019a)  
398



399  
400



401  
402  
403  
404  
405  
406  
407  
408  
409  
410  
411

**Fig. 4.** Overview of final surface structures ( $t = 48$  h) of selected experiments with basin geometries 1 and 6 illustrating general model behaviour. (a-b) Models A and F from series I, tilted by  $1^\circ$ . (c-d) Models K and U from series II, tilted by  $3^\circ$ . Note that the initial distances between the surface markers was not constant (see description in Section 2.4): the markers in (a) and (b) are almost in situ.

### 412 3.2. Quantitative results from Series I (1° basin tilt models)

413

414 From visual inspection on top view imagery (section 3.1), we identified that the degree of margin tilt  
415 is an important factor in our models: the models with 1° basin tilt from Series I exhibit very limited  
416 deformation. Accordingly, the DEM analysis generally did not show a significant enough topographic  
417 signal in most models. By contrast, PIV analysis was sensitive enough to provide some useful  
418 insights into the evolution and deformation of the 1° basin tilt models and its results are reported  
419 here (Figs. 5 and 6).

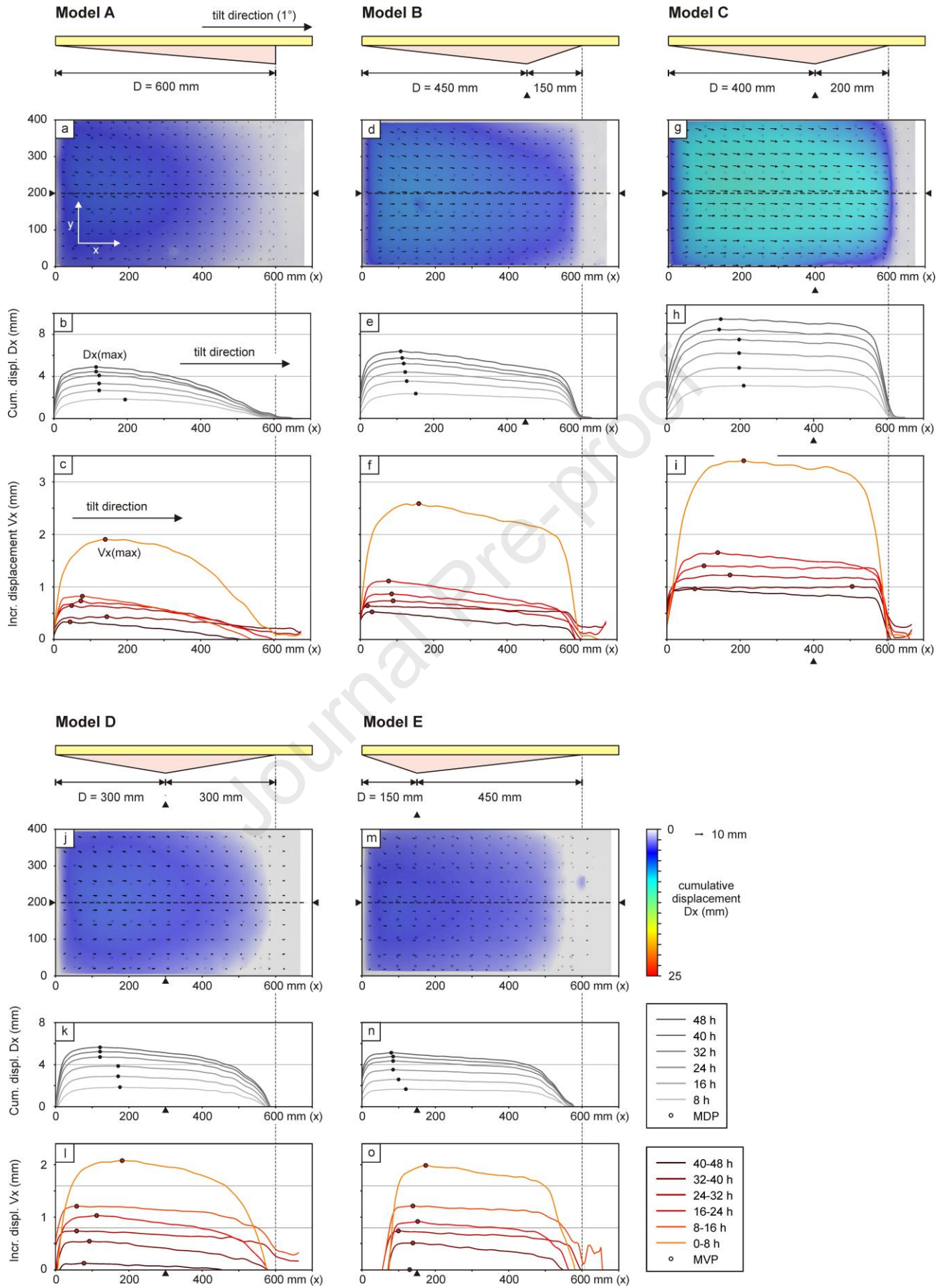
420

421 Models A-E from Series I all (with constant mean model salt thickness) showed very similar  
422 displacement patterns (Fig. 5). Deformation was registered above the whole extent of the model salt  
423 basins and the displacement curves (both the  $D_x$  and  $V_x$  curves) generally formed a plateau  
424 between an upslope increase in displacement and a downslope decrease in displacement. These  
425 sections of the curves represent an upslope extensional domain, and a downslope compressional  
426 domain with a translation-dominated domain in between. The plateau itself was often slightly tilted  
427 towards the downslope end of the model, indicating a very minor ( $< 1\%$ ) distributed shortening  
428 within the translation domain. Only Model A deviated from this pattern, as it developed bell-shaped  
429 displacement curves with the top towards the upslope end of the profiles indicating a general  
430 downslope decrease in displacement representing more distributed shortening (Fig. 5a-c). We  
431 found that maximum final displacements ( $D_{x_{max}}$ ) generally ranged between 5 and 7 mm, with a  
432 maximum for Model C, in which  $D_{x_{max}}$  was ca. 8 mm. Importantly, the  $V_x$  plots show that a major  
433 part of this displacement occurred in the earliest phases of the model runs, after which downslope  
434 displacement rates quickly decreased before stabilizing towards the end of the experimental run  
435 (Fig. 5c, f, i, l, o). Notably, the translation domain was established very early during the evolution in  
436 most models (i.e. during the first 8 h increment) as manifested by a plateau in the first member of  
437 the array of  $V_x$  curves. However,  $V_x$  values in the translation domain of each model slowly  
438 decreased towards the downslope end of the model, as also indicated by the upslope location of the  
439 MVP.

440

441 PIV analysis of Models F-J from Series I (with varying mean model salt volumes and maximum  
442 basin depths) revealed displacement patterns with very similar styles to those observed in Models  
443 A-E, i.e. plateau and bell-shaped displacement curves (Figs. 5 and 6). Models F-H, with thicker  
444 mean model salt thicknesses) showed significantly higher overall displacements compared to  
445 Models A-E (final  $D_{x_{max}}$  value between 15 and 20 mm versus 5-8 mm, Figs. 5, 6a-g). By contrast,  
446 the total displacement values in the shallow model salt basins of Models I and J were relatively low  
447 (final  $D_{x_{max}}$  values of ca. 3.5 and 2, respectively). While similar to models A-E in that displacement  
448 generally decelerated over the model runs, the translational domain seems to be established slightly  
449 later, i.e. during the second increment of deformation (8-16 h), as indicated by the more bell-shaped  
450 first member of the array of  $V_x$  curves (Fig. 5). Also in these models, the  $V_x$  values in the  
451 translational domain gently decreased towards the downslope end of the model, and the MVP was  
452 situated upslope.

453

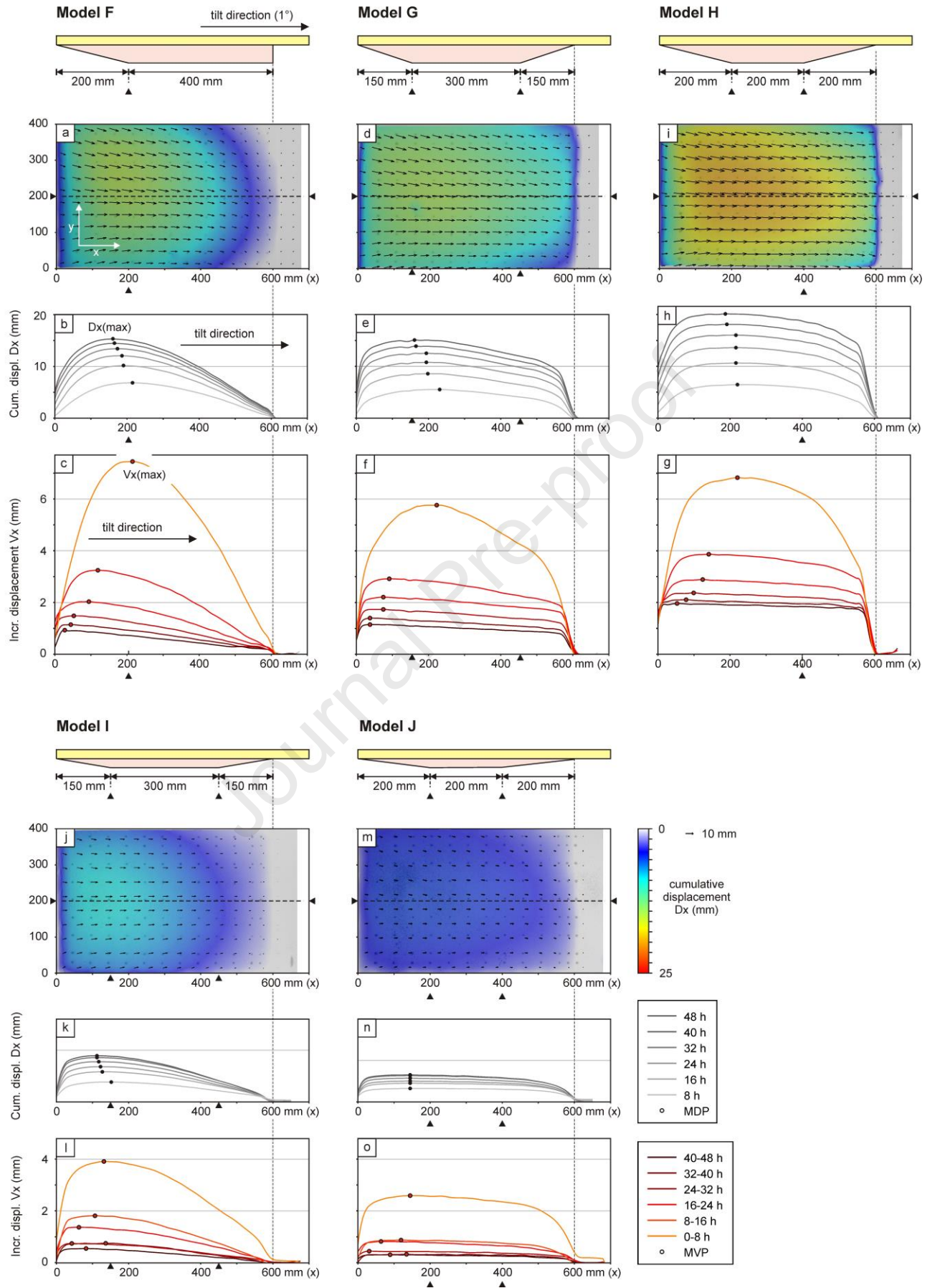


455  
456  
457  
458  
459  
460

**Fig. 5.** PIV-derived surface displacements of models A-E from series I ( $1^\circ$  basin tilt, basin shapes 1-5, with constant mean model salt thickness), shown in both map view ( $D_x$  only) and plotted on along-axis profiles (both  $D_x$  and  $V_x$ ). MDP: maximum displacement point. MVP: maximum displacement point. For more details on definitions, see Fig. 3.

Journal Pre-proof





462  
463  
464  
465  
466

**Fig. 6.** PIV-derived surface displacements of models F-J from series I ( $1^\circ$  basin tilt, basin shapes 6-10, with constant mean model salt thickness), shown in both map view ( $D_x$  only) and plotted on along-axis profiles (both  $D_x$  and  $V_x$ ). MDP: maximum displacement point. MVP: maximum displacement point. For more details on definitions, see Fig. 3.

Journal Pre-proof

### 467 **3.3. Quantitative results from Series II (3° basin tilt models)**

468

469 For this model series both topography (SfM) and displacement (PIV) analysis yielded good results.  
470 We start each of the following sections accordingly with the results from topography analysis and  
471 then show the results for displacement analysis.

472

473

#### 474 **3.3.1 Models K-O (with constant mean model salt thickness)**

475

476 Based on visual inspection of map view imagery in section 3.1 we showed that the models with 3°  
477 basin tilt developed distinct deformation features in the shape of extensional structures in the  
478 upslope parts, and contractional structures downslope (Fig. 4c, d). These general features are also  
479 clearly visible in the topography analysis results (map view and section view) from models A-E (Fig.  
480 7), but we notably found some systematic topographic variations associated with the location of the  
481 model salt basin depocenter.

482

483 In section view we observed a general increase in total mass displacement when the model salt  
484 basin depocenter was situated higher upslope (from ca. 430 mm<sup>2</sup> to 690 mm<sup>2</sup> in section, Fig. 7).  
485 This trend also correlates with an increase in maximum subsidence in the extensional domain at the  
486 upslope end of the models if the model salt depocenter is positioned higher upslope (from ca. 2.9  
487 mm to 5.5 mm), whereas the maximum uplift recorded in the downslope part was simultaneously  
488 decreased (from ca. 8.4 to 6.5 mm) (Fig. 7). Yet within Models K-O, the loci of maximum vertical  
489 displacement remained rather stable with changing depocenter locations (Fig. 7). Furthermore, we  
490 found that the point of zero vertical motion (PZVM) was found higher upslope in models with a  
491 higher upslope model salt depocenter (Fig. 7). Here it is worth noting that the PZVM was situated  
492 upslope of the model salt depocenter in Models K-M (Fig. 7a-c), but in Models N and O, the PZVM  
493 was higher upslope than the model salt basin depocenter (Fig. 7d-e) so that the PZVM “overtook”  
494 the upward model salt depocenter shift from Model K to Model O. Finally, models with a downslope  
495 depocenter allowed material to move farther downslope, out of the basin (e.g. Model K, Fig. 7a).

496

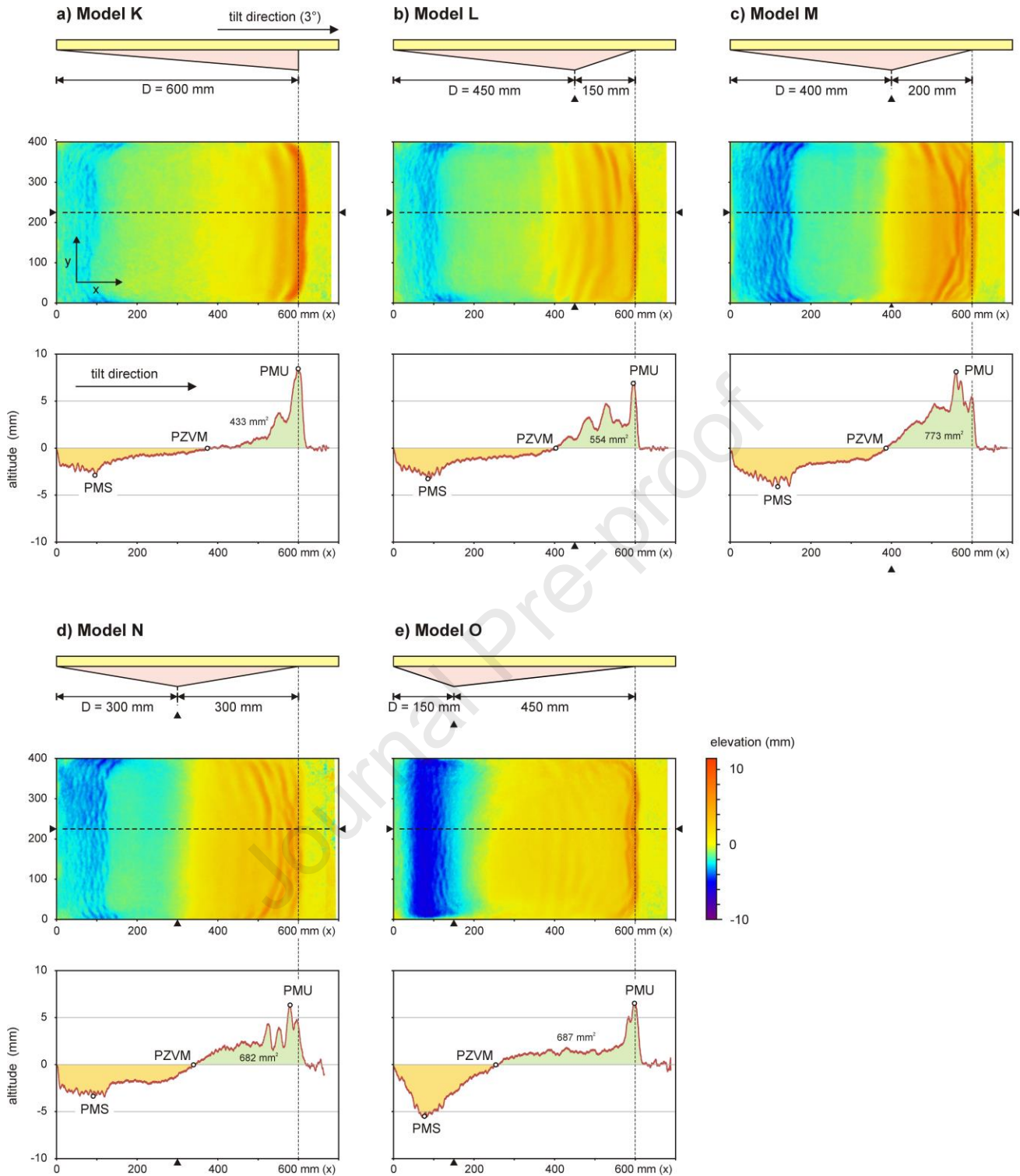
497 Using the topographic parameters allows a detailed quantification of deformation in these models,  
498 yet these parameters do not fully capture specific aspects. For instance, the surface of the  
499 translational domain in Models K-O, is clearly tilted due to upslope subsidence and downslope uplift  
500 (Fig. 7). In some cases the translational domain also showed the development of a “slope break” as  
501 the downslope part of the translational domain is tilted to a higher degree with respect to the  
502 upslope part (Models L-N, Fig. 7b-d). It should also be noted that the topographic parameters in  
503 Model C (basin shape 3) are systematically slightly more pronounced than in the other models (Fig.  
504 7c).

505

506

507





508  
 509  
 510  
 511  
 512  
 513  
 514  
 515

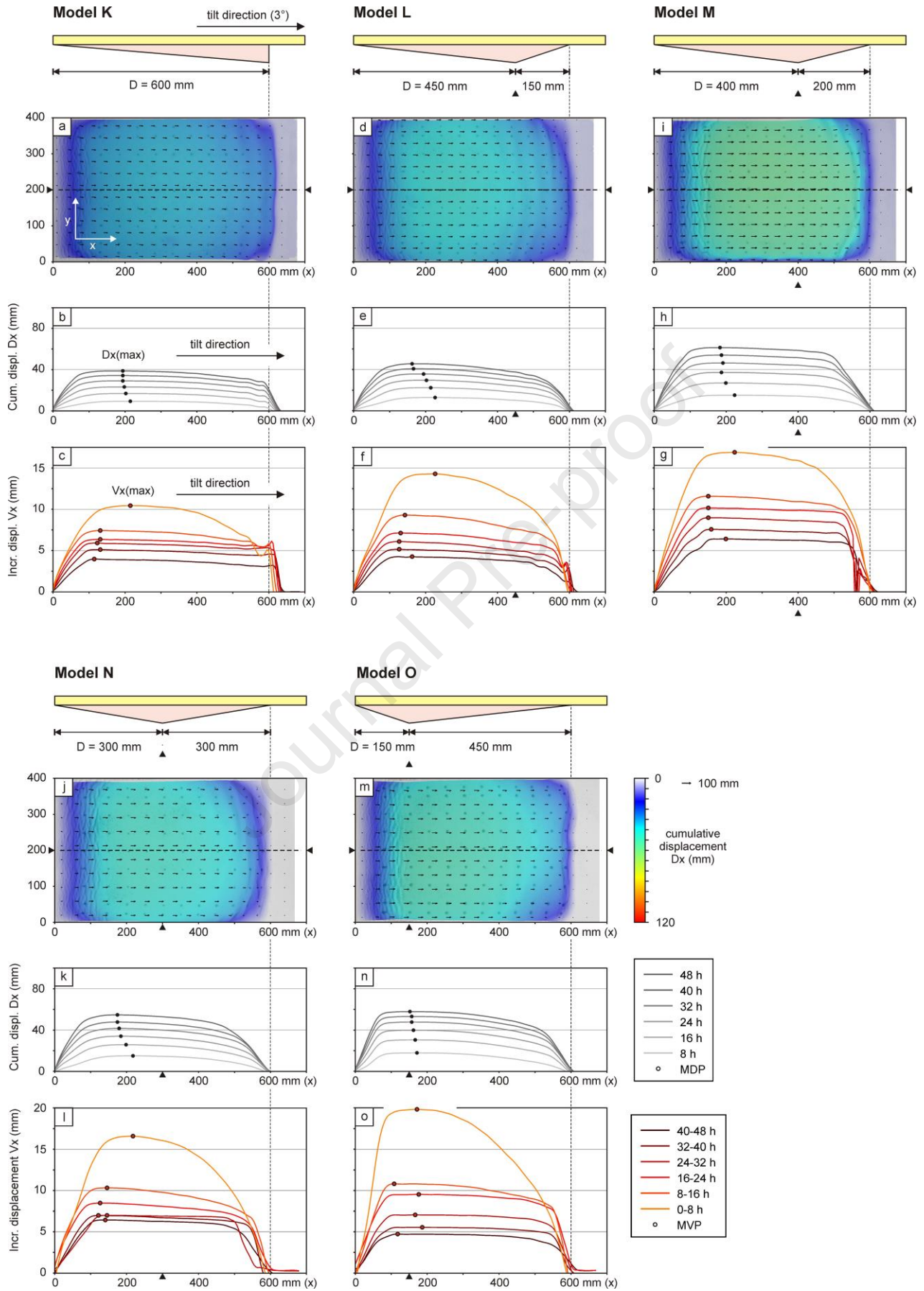
**Fig. 7.** Final normalized topography of Models K-O from Series II ( $3^\circ$  basin tilt, basin shapes 1-5 with constant mean model salt thickness) in map view and along a central section. PZVM: point of zero vertical motion, PMS: point of maximum subsidence, PMU: point of maximum uplift. For more details on definitions, see Fig. 3.

516 In general, 3° basin tilt models accumulated higher displacements compared to the 1° basin tilt  
517 models. While the 1° tilt models with constant mean model salt thickness (Models A-E from Series I)  
518 registered final cumulative downslope displacements ( $Dx_{max}$ ) of 5-8 mm (section 3.2, Fig. 4), the  
519 equivalent 3° basin tilt Models K-O from series II accumulated up to ca. 50 mm downslope  
520 displacement (Fig. 8). Another contrast with the 1° models is that the final cumulative displacement  
521 ( $Dx_{max}$ ) profiles of Models K-O are distinctly plateau-shaped, indicating the occurrence of three salt  
522 tectonic domains (upslope extension, mid-slope translation and downslope contraction). Only a hint  
523 of the bell-shaped displacement curves observed in Models A-E can be seen in the initial phases as  
524 recorded by the  $V_x$  plots (Fig. 8c, f, g, l and o), hinting that the development of the salt tectonic  
525 domains was not instantaneous.

526  
527 Similar to the topographic analysis, detailed PIV analysis of Models K-O reveals clear correlations  
528 between model salt basin depocenter location and displacements. We found that models with a  
529 more downslope depocenter produced less displacement than those with a more upslope  
530 depocenter: Model K registered a  $Dx_{max}$ -value of 45 mm, whereas Model O registered a  $Dx_{max}$ -value  
531 of ca. 55 mm (Fig. 8i). An exception in this trend is Model M with a  $Dx_{max}$ -value of 70 mm (Fig. 8i-g)  
532 and it may be noted that this particular model salt basin geometry also registered anomalously high  
533 displacements in Model C with 1° basin tilt (Fig. 5g-i). All of Models K-O showed an upslope  
534 migration of the MDP over time (Fig. 8b, e, h, k, n).

535  
536 As observed in the models from Series I downslope displacement was highest during the early  
537 model stages before it gradually waned towards the end of the model run (Figs. 9 c, f, g, l, o, 8c, f,  
538 g, l, o). Similar to the  $Dx_{max}$  values, the  $V_{max}$  values also increased when the model salt basin  
539 depocenter was situated higher upslope (from ca. 11 mm in Model K to ca. 20 mm in Model O, Figs.  
540 8c and o, respectively). Furthermore, with the exception of Model O, the MVP systematically  
541 showed an upslope migration during early model evolution, often followed by a reverse, downslope  
542 path during later stages (Figs. 8c, f, g, l, o).

543  
544



546  
547  
548  
549  
550  
551  
552

**Fig. 8.** PIV-derived surface displacements of models K-O from series II ( $3^\circ$  basin tilt, basin shapes 1-5, with constant mean salt thickness), shown in both map view ( $D_x$  only) and plotted on along-axis profiles (both  $D_x$  and  $V_x$ ). MDP: maximum displacement point. MVP: maximum displacement point. For more details on definitions, see Fig. 3.

Journal Pre-proof

**3.3.2. Models U-Y (with varying mean model salt thickness)**

553

554

555

556

557

558

559

560

561

562

563

564

565

566

567

568

569

570

571

572

573

574

575

576

577

578

579

580

581

582

583

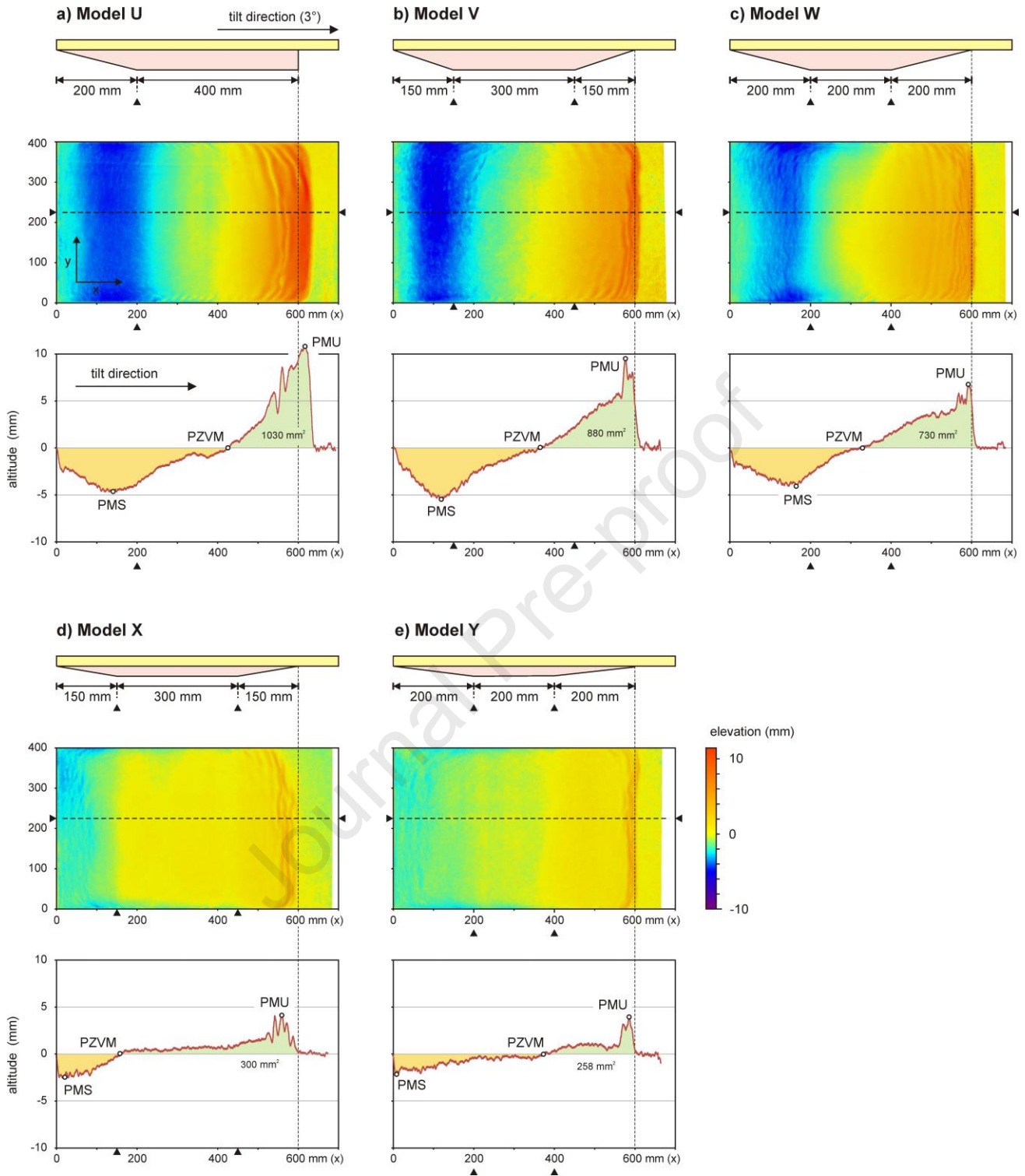
584

As illustrated in sections 3.1 and 3.2, a higher mean model salt thickness caused increased deformation in our models. This effect was well captured by the final topography of models U-Y from Series II (Fig. 9). Map and profile views of the final normalized topography of these models with 3° basin tilt and varying mean model salt thickness show that Model U (with the highest mean model salt thickness) developed the most pronounced relief (with uplifts up to ca. 12 mm, Fig. 9a). Subsequent Models V and W with gradually decreasing mean model salt thickness also developed gradually less relief (uplifts of ca. 9 mm and 7 mm, respectively, Fig. 9b and c). Furthermore, the very low mean model salt thickness in Models X and Y resulted in very limited relief (Fig. 9d, e). This trend is also captured by the total mass displacement analysis, which consistently drops with decreasing model salt thickness, and ranges from ca. 1000 mm<sup>2</sup> in model U to 250 mm in Model Y (Fig. 9).

Due to the dominance of the mean model salt thickness in Models U-Y, we did not systematically analyze the various topographic parameters. Yet we identified some potential indications of basin shape influence on final topography. In Models U-W we observed an upslope shift of the PVMZ as the downslope basin floor inclination decreases, analogue to the effect of the model salt basin depocenter location seen in Models K-O (Fig. 7).

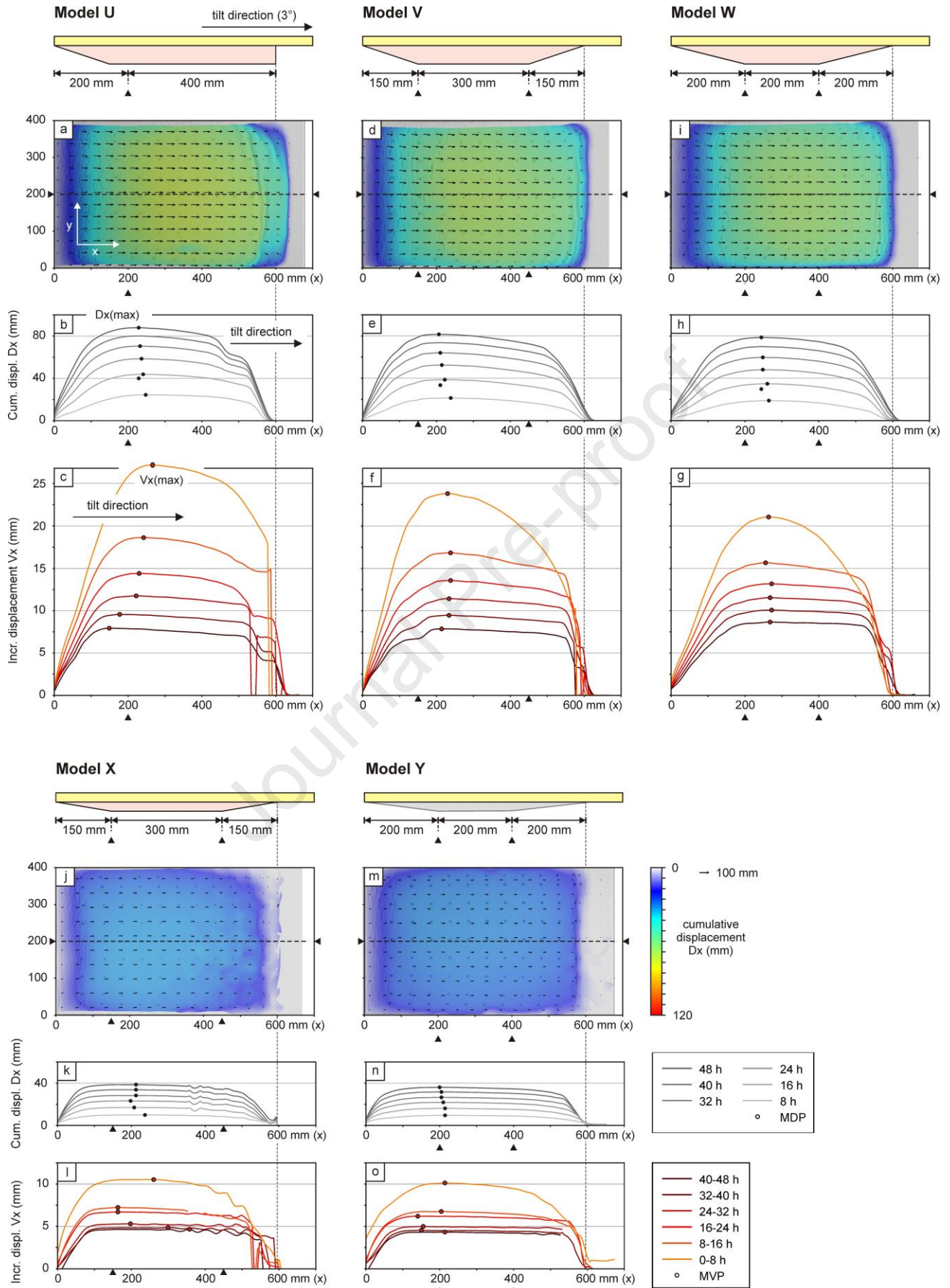
PIV analysis of Models U-Y (Fig. 10) revealed similar trends to those observed in their 1° basin tilt equivalents Models F-J (Fig. 6): higher mean model salt thicknesses cause increased displacement. Similar to the total mass displacement analysis from the topography analysis (Fig. 9), the Dx and Vx-values from Models U-Y show a very clear correlation (decreasing from ca. 90 to 35 mm and 28 to 10 mm, respectively, Fig. 10). A contrast between Models U-Y and Models K-O is that the MDP and MVP remain rather stable in the former (Fig. 10). Yet the initial displacement curves (Vx) did show similar bell-shapes to those in models K-O, which later on developed into plateau-shaped curves with a slight decrease in displacement values towards the downslope end of the model salt basins (Figs. 8 and 10).





585  
586  
587  
588  
589  
590  
591

**Fig. 9.** Final normalized topography of Models U-Y from Series II (3° basin tilt, basin shapes 6-10 with varying mean model salt thickness) in map view and along a central section. PZVM: point of zero vertical motion, PMS: point of maximum subsidence, PMU: point of maximum uplift.





593 **Fig. 10.** PIV-derived surface displacements of models U-Y from series II ( $3^\circ$  basin tilt, basin shapes  
594 6-10 with varying mean model salt thickness), shown in both map view (Dx only) and plotted on  
595 along-axis profiles (both Dx and Vx). MDP: maximum displacement point. MVP: maximum  
596 displacement point. For more details on definitions, see Fig. 3.

Journal Pre-proof

## 597 3.4 Synthesis of key model results

598

### 599 3.4.1. Topography (Models K-O and U-Y)

600

601 In Fig. 11 we provide a systematic overview of the cross-correlation of key parameters from the  
 602 topographic analysis with the geometric parameters of our models. We found a very clear  
 603 correlation between mean model salt thickness and mass displacement (Fig. 11a). Note that due to  
 604 the very limited topographic development in the 1° models from series II (see section 3.2), these are  
 605 not included in this overview, but this alone also indicates the strong effect of basin tilt on model salt  
 606 tectonic deformation. When isolating the models with a constant mean thickness and a 3° tilt  
 607 (Models K-O), we can extract the effect of basin shape (i.e. model salt basin depocenter) on salt  
 608 tectonic deformation.

609

610 Within this context, a downslope model salt basin depocenter caused a decrease in mass  
 611 displacement (Fig. 11b). This was associated with an increase in maximum uplift, as well as a  
 612 decrease in maximum subsidence (Fig. 11c). Yet the locations of maximum uplift and subsidence  
 613 remained fairly constant (Fig. 11d). We also found that the PZVM was situated higher upslope as  
 614 the model salt depocenter was located higher upslope as well, but the PZVM “overtook” the upward  
 615 shift of the depocenter from Model K to model O, so the PZVM became situated higher upslope  
 616 than the model salt basin depocenter (Fig. 11e). We also observed that a downslope model salt  
 617 depocenter more readily allows material to move out of the basin (Fig. 11f).

618

619

### 620 3.4.2. Surface displacement (Series I and II)

621

622 Similar to the results from the topography analysis, the PIV-derived maximum and mean cumulative  
 623 displacement data ( $Dx_{max}$  and  $Dx_{mean}$ ) from Series I and II clearly show the dominant influence of  
 624 firstly basin tilt and secondly mean model salt thickness on the degree of deformation in our models  
 625 (Fig. 12a and b). It may be noted that these trends are very similar when considering both  
 626 measures, showing that  $Dx_{max}$  is a good proxy for  $Dx_{mean}$  in these models.

627

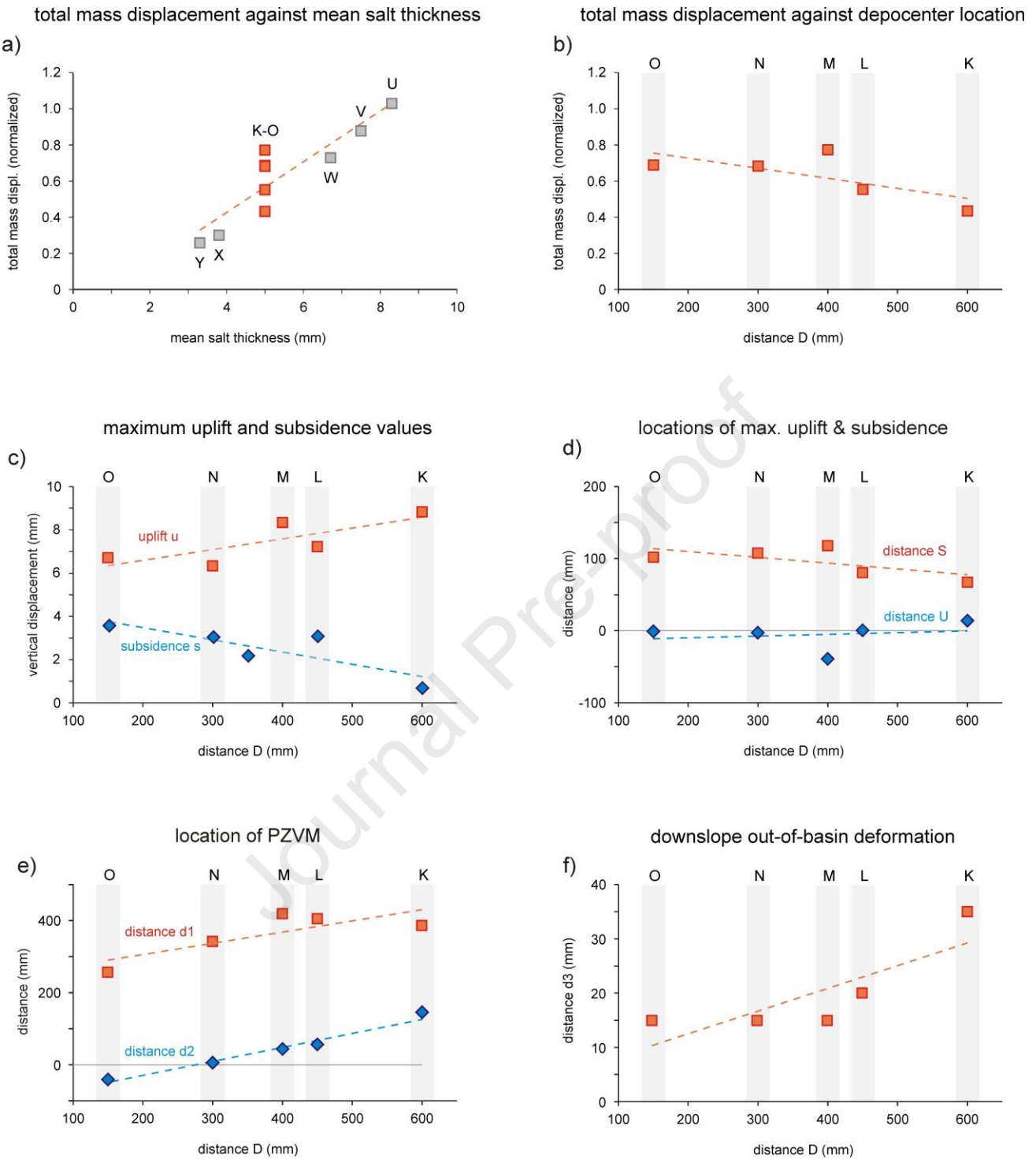
628 When only considering Models K-O with constant mean model salt thickness and 3° basin tilt to filter  
 629 out the effects of basin tilt and model salt thickness, we found that final cumulative displacement is  
 630 higher when the model salt basin depocenter is situated higher upslope (Fig. 12c), a result that is  
 631 very similar to the mass displacement from topographic analysis (Fig. 12b). The same trend  
 632 emerged from the  $Vx$  data, although the correlation between depocenter became less strong  
 633 towards the end of the model runs, as general displacement rates dwindled (Fig. 12d). In general  
 634 the decay of the maximum displacement rate over time for both the Series I and Series II models is  
 635 quasi exponential, not reaching a steady state rate at the end of the experimental run (Fig. 12e).  
 636 Furthermore, the location of the MDP in Models K-O was correlated to the model salt basin  
 637 depocenter as the MDP was found higher upslope when the depocenter was situated higher  
 638 upslope (Fig. 12f). A similar trend was also found in models U-W (Section 3.3.2, Fig. 9a-c).

639

640 Finally, the evolution of the MVP as summarized in Fig. 12g, firstly showing that the initial  
 641 displacement rates were higher for models with the model salt basin depocenter higher upslope.  
 642 Subsequently displacement rates decrease over time, while the MVP generally migrates upslope.  
 643 This upslope migration of the MVP, which in some cases is reversed in the later stages of the model  
 644 run (Fig. 12g).

645

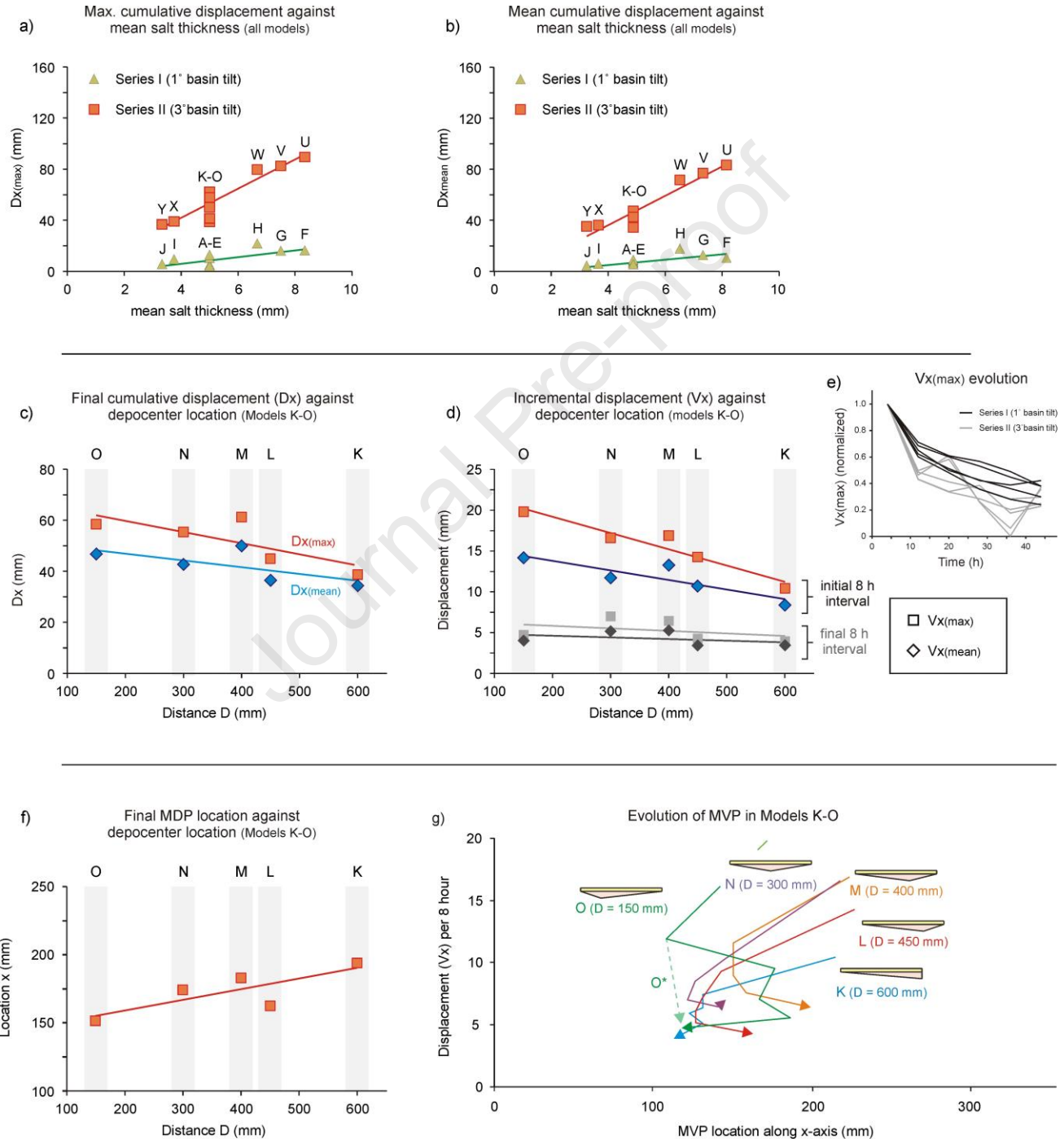
646



647  
648  
649  
650  
651  
652  
653  
654  
655  
656

**Fig. 11.** Overview of results of topography analysis in experiments from Series II with 3° basin tilt (see Fig. 3f for definitions of the various topographic parameters). (a) Total mass displacement against mean model salt thickness in all Series II models. (b-f) Detailed analysis of models K-O with constant mean layer thickness but different model salt basin decenter locations, where the model salt basin decenter location is defined by distance D. (b) Total mass displacement against model salt basin decenter location (distance D). (c) Maximum uplift (u) and subsidence (s) against model salt basin decenter location. (d) Location of maximum uplift (U) and subsidence (S) against model salt basin decenter location (e) Location of the point of zero vertical motion (PZVM),

657 measured from the upslope basin end (d1) and measured from the model salt basin depocenter  
 658 location (d2), against model salt depocenter location. (f) Maximum downslope propagation of  
 659 deformation (d3) from the downslope basin end against model salt basin depocenter location. The  
 660 capital letters in the plots indicate what model the date are from.  
 661  
 662  
 663  
 664  
 665



666  
 667

668 **Fig. 12.** Overview of PIV-derived surface displacement analysis on experiments from Series I and II  
669 (For details on the various definitions, see Fig. 3.) (a-b) Relations between and PDMS volume and  
670 maximum cumulative displacement ( $Dx_{max}$ ) and total cumulative displacement ( $Dx_{mean}$ ), (c-g)  
671 Overview of surface displacement results from Models K-O from Series II ( $3^\circ$  basin tilt, constant  
672 mean model salt thickness) as a function of model salt basin depocenter location (defined by  
673 distance  $D$ , see Fig. 3f). (c) Final maximum and mean cumulative displacement values ( $Dx_{max}$  and  
674  $Dx_{mean}$ ) against model salt basin depocenter location. (d) Evolution of maximum and mean  
675 incremental displacement values ( $Vx_{max}$  and  $Vx_{mean}$ ) against model salt basin depocenter location.  
676 (e) Comparison (normalized) of maximum incremental displacement ( $Vx_{max}$ ) evolution in Models A-E  
677 and K-O. (f) Relation between the location of the maximum displacement point (MDP) and basin  
678 depocenter location. (g) Evolution of the maximum velocity point or MVP (location and associated  
679  $Vy_{max}$ ) over time for Models K-O. The arrows indicate the direction of evolution. O\*: Note that the  
680 continuous line for Model O shows the real data that may contain a slight error, where the dotted  
681 line indicates a path that would be more in line with the other experiments. The capital letters in the  
682 plots indicate what model the data are from. For more details on definitions, see Fig. 3.  
683  
684

## 685 4. Discussion

686

### 687 **4.1. Effects of margin tilt and mean salt thickness**

688

689 Our model results illustrate a very strong correlation between the amount of accumulated horizontal  
690 displacement or total mass displacement and the tilt angle of the basin: a higher degree of tilting  
691 induces more deformation, whereas little deformation is observed with a low degree of tilt (Figs.  
692 11a, 12a and b). This is clearly caused by the forces acting on the models in combination with  
693 rheology, in particular that of the model salt, becoming less stable due to larger gravitational forces  
694 acting along steeper slopes and is thus more likely to start moving downslope (e.g. Brun & Fort  
695 2011; Peel 2014). Yet this effect diminished over time in the experiments, as material moved  
696 downslope so that the system ran out of potential energy (i.e. loss of gravitational head) and started  
697 to stabilize (yet not fully settled, and will probably never do so due to basal drag, Fig. 12e), as is  
698 consistent with the instant tilting boundary condition (Ge et al., 2019b).

699

700 The second important factor in our experiments is mean salt thickness, which itself is a general  
701 constraint based on the basin's geometry (i.e. the general salt basin depth) and the available  
702 volume of salt in a system. The thicker the overall salt layer, the less stable the system is when it  
703 starts to tilt due to reduced shear strength and consequent reduced coupling with the base of the  
704 basin (e.g. Brun & Fort 2011). Because the viscous nature of the model salt (i.e. the PDMS  
705 silicone), its strength is directly related to forces driving its deformation and the resulting shear rate.  
706 Thicker salt layers under constant gravitational forces are therefore weaker because shear is more  
707 distributed and shear rates consequently lower.

708

709

### 710 **4.2. Influence of salt basin depocenter location**

711

712 Although basin tilt and mean salt thickness dominate our model results, the experiments with a  
713 constant mean salt thickness and 3° basin tilt (Models K-O) allow us to assess the secondary effects  
714 of basin shape (i.e. depocenter location) on salt tectonics (summarized in Fig. 13).

715

716 On a large scale, we found a decrease in total mass displacement when the salt basin depocenter  
717 is shifted downslope (Figs. 7 and 11b). The same correlation exists between total cumulative  
718 displacement and salt basin depocenter location, supporting this observation (Figs. 8 and 12c, d).  
719 The fact that cumulative displacement decreased when the salt basin depocenter was situated more  
720 downslope was likely linked to the associated distribution of potential energy in the system; the  
721 higher upslope the depocenter is situated, the more (instable viscous) material is available upslope,  
722 the pressure of which more readily overcomes basal drag, causing enhanced downslope  
723 displacement and subsidence in the upslope parts (Figs. 7, 8, 11b and 12c, d).

724

725 A more upslope salt basin depocenter location is also strongly associated with the PZVM and MDP  
726 sitting higher upslope (Figs. 11e, 12f, 13). This trend is accompanied by an increase in maximum  
727 subsidence in the upslope extension domain, made possible by the increased thickness of the salt  
728 basin there, which can be readily evacuated to leave more space for subsequent subsidence (e.g.  
729 Dooley et al. 2017, Pichel et al. 2018, Fig. 11c). We simultaneously found less localized uplift (lower  
730 maximum uplift values) in the downslope domain (Fig. 11c), but the increased mass displacement  
731 caused a wider, more general uplift there (Figs. 7, 13). This is because when the depocenter is  
732 higher upslope, the downslope part of the basin becomes relatively shallow. As a result, the thinner  
733 salt analogue does not allow deformation in the brittle layer due to increased brittle-viscous coupling  
734 and basal drag, causing a wider thickening and uplift (similar to the models by Dooley et al. 2017  
735 and Pichel et al. 2018).

736



737 Basal drag may be causing the PZVM shift in models U-W as well (Figs. 9a-c, 10a-i), even though  
738 these models also have varying mean salt thicknesses. The braking effect of basal drag is also  
739 clearly seen in experiments with a maximum 5 mm basin depth (Figs. 9d, e, 10j-o), and is the  
740 reason for the decreased propagation of deformation out of the basin in Models K-O when the  
741 depocenter is situated higher upslope, since material is less effective in moving over the thinner  
742 viscous layer downslope (e.g. Dooley et al. 2017, 2018, Fig. 13).

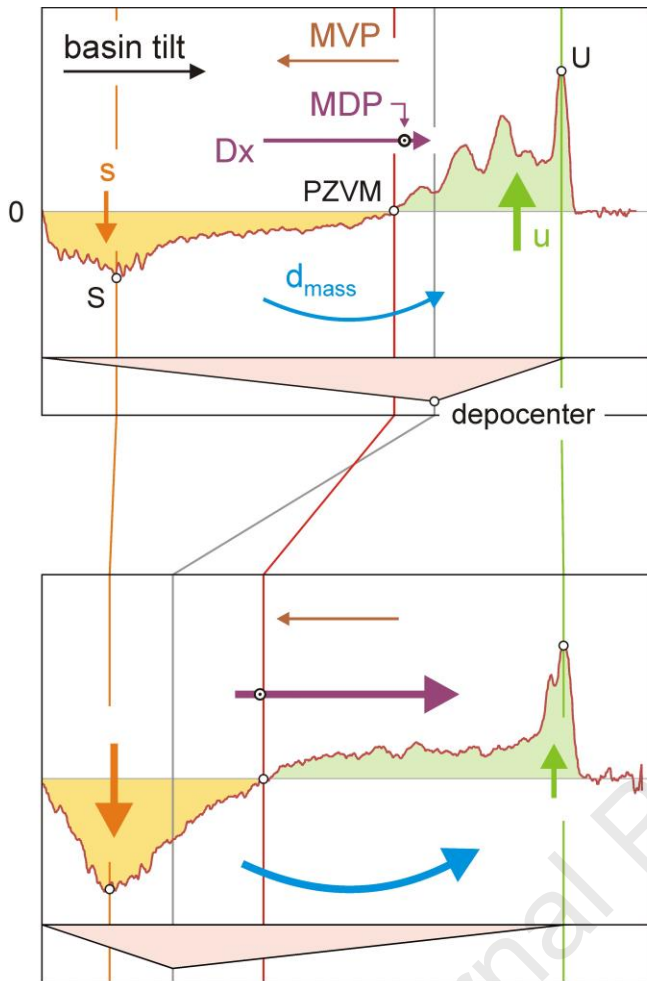
743  
744 A further insight from the topography analysis is that the translational domain, which moves without  
745 significant internal horizontal deformation, does actually tilt due to upslope subsidence and  
746 downslope uplift (Figs. 7). This contrast can be so significant that the sand cover in the translational  
747 domain “buckles” as observed in Models L-N (Fig. 7b-d). Both horizontal and vertical translational  
748 motions are thus clearly accommodated by the deforming viscous layer below. The exact  
749 expression of this “bucking” or “contractional hinge” (Hudec & Jackson 2017) seems to be a factor  
750 of salt basin depocenter location as thinner downslope salt thicknesses leads to increased basal  
751 drag and wider uplift zones (Fig. 13).

752  
753 Also, the location of maximum uplift and subsidence remains rather stable (Figs. 11d, 13). The point  
754 of maximum uplift is always situated near the downslope end of the salt basin, downslope of which  
755 deformation is almost impossible. Downslope migration of the maximum subsidence point is  
756 probably prohibited by the relatively stable translational domain, as the downslope motion of this  
757 domain is controlled by the contraction at the downslope edge of the basin. Yet these insights  
758 represent the final model state and we may expect some slight variation over time, although the  
759 general trend we observe most likely remains valid.

760  
761 A final point of attention is that displacement was anomalously high in both Models C and M with  
762 salt basin shape 3 (Figs. 5i-g, 7c, 8i-g, 11b-e, 12 c and d). The fact that this occurred in two models  
763 might indicate that it was no strange discrepancy due to for instance model preparation. Perhaps  
764 basin shape 3 is close to the optimal basin shape for accommodating gravity-gliding type salt  
765 tectonics. The salt thickness on both sides of the salt basin depocenter is relatively high, but the  
766 slight upslope depocenter location would then still allow for relatively high degrees of instability.

767  
768





#### downslope salt basin depocenter:

- ▶ PZVM upslope from depocenter
- ▶ moderate subsidence (s)
- ▶ very high uplift (u)
- ▶ low horizontal displacement (Dx)
- ▶ MDP relatively downslope
- ▶ MVP generally migrates upslope over time
- ▶ moderate mass displacement ( $d_{\text{mass}}$ )

#### upslope salt basin depocenter:

- ▶ PZVM downslope from depocenter
- ▶ very high subsidence (s)
- ▶ high uplift (u)
- ▶ high horizontal displacement (Dx)
- ▶ MDP relatively upslope
- ▶ MVP generally migrates upslope over time
- ▶ high mass displacement ( $d_{\text{mass}}$ )
- ▶ stable point of max. vertical motion (S, U) compared to downslope depocenter models

769  
770  
771  
772  
773  
774  
775  
776  
777  
778  
779

**Fig. 13.** Impact of basin geometry (grey shape) on salt tectonics from PIV and topographic analysis on Series II experiments K-O ( $3^\circ$  basin tilt, constant mean salt thickness). The red curve indicates final model topography along the central model axis, and the orange and green areas indicate the area of subsidence and uplift in profile, respectively. PZVM: point of zero vertical motion, MDP: maximum displacement point, MVP: maximum velocity point. For more details on definitions, see Fig. 3.

### 780 4.3. Development of salt tectonic domains

781

782 Most of our models developed the distinct gravity-gliding domains typical for gravity-gliding systems  
783 (i.e. upslope extension, mid-slope translation and downslope contraction, e.g. Demercian et al.  
784 1993; Spathopolous 1996; Rowan et al. 2004; Brun & Fort 2011; Dooley et al. 2017). Yet these  
785 domains are generally not established during the initial phases of our models, as expressed by the  
786 initial bell-shape of the  $V_y$ -profiles, and in some of the  $1^\circ$  basin tilt models from Series I, they did not  
787 develop at all (Figs. 5, 6, 8, 10).

788

789 We propose that the brittle sand layer covering the salt basin stabilizes the system as it forms a  
790 brittle seal with finite yield strength that prevents immediate deformation due to salt instability as the  
791 basin is (slightly) tilted (Ritter et al., 2018, compare to the Series III models without sand cover in the  
792 Appendix). In our  $1^\circ$  margin tilt experiments this stabilizing effect seems to largely balanced the  
793 gravitational forces, allowing only limited deformation to occur (Figs. 4a, b, 5, 6). Yet in the  $3^\circ$  basin  
794 tilt models, gravitational forces readily overcame the peak strength of the sand layer, enabling the  
795 development of the typical salt-tectonic domains (Figs 4c, d, 7-10).

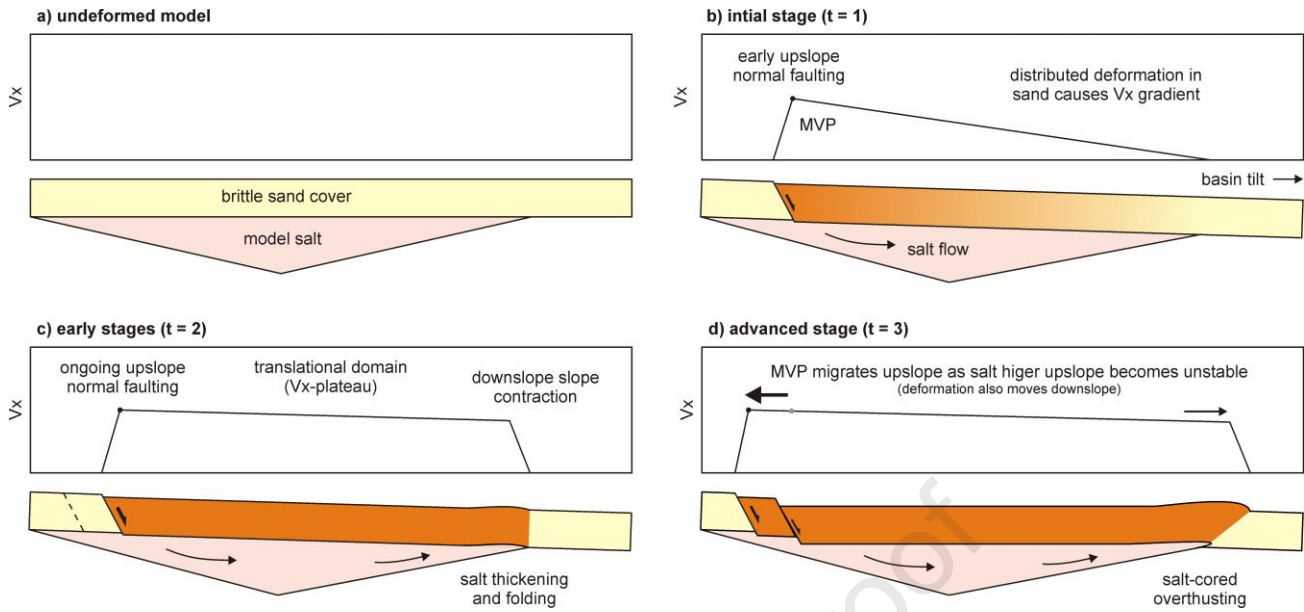
796 The  $V_x$  results reveal how this establishment of the salt tectonic system occurs in more detail (Fig.  
797 14). Initially, the tilting of the basin causes displacement without a clear plateau and the highest  
798 displacements situated upslope, where extensional faulting occurs. However, no sufficient force is  
799 yet available to cause contractional deformation in the downslope part of the salt basin, hence the  
800 decrease in displacement towards the downslope end of the salt basin (Fig 14b). As upslope  
801 displacement continues, sufficient stress builds up to induce contraction in the downslope domain.  
802 As a result, a translational domain with near-constant displacement can be established (Fig. 14c).  
803 Subsequently, as material moves downslope, the parts of the upslope domain that were previously  
804 supported by the now fully mobile sand cover of the translational domain become unstable as well,  
805 causing an upslope shift in maximum displacement rates (i.e. the MVP migrates upslope, Figs. 12g,  
806 14d). Next to this inferred support by the translational domain, basal drag at the upslope part of the  
807 salt basin probably decelerates downslope salt flow there as well, contributing to the delayed  
808 extension captures in our  $V_x$  plots (Dooley et al. 2017). Similar migration of displacement patterns  
809 was also observed in models by Quirk et al. (2012) and Ge et al. (2019b).

810

811 Finally, in some models, we observed a late downslope migration of the MVP (Fig. 12g). This may  
812 be due to the exhaustion of mobile model salt in the upslope domain, so that further deformation  
813 could only occur farther downslope.

814

815



816  
817  
818  
819  
820  
821  
822  
823  
824

**Fig. 14.** Development of the various domains of a salt tectonic system as derived from the PIV-derived incremental displacement ( $V_x$ ) profiles shown in Figs. 5, 6, 8 and 10. MVP: maximum velocity point. Red indicates downslope displacement.

#### 825 4.4. Model limitations

826

827

828 Although our simple model set-up allows us to extract a number useful insights into the effects of  
829 basin tilt and salt basin geometry (i.e. mean salt thickness and depocenter location), some  
830 limitations exist that need to be taken into account.

831

832 Firstly, the basin tilt we applied in our models was instantaneous, whereas margin tilt due to  
833 differential thermal subsidence along a passive margin is considered to be gradual. Although  
834 instantaneous basin tilting has often been used in previous modelling studies (e.g. Brun & Fort  
835 2004, Fort et al. 2004a, b, Quirk et al. 2012; Dooley et al. 2018), the application of a gradual basin  
836 tilt might have been more realistic (e.g. Ge et al. 2019a, b; Warsitzka et al. 2021). However, our  
837 modelling results show that small degrees of tilting do only cause very limited deformation and most  
838 deformation takes place when tilt angles are higher. Therefore the discrepancy between natural  
839 examples and our models is probably less distinct than might appear. One could even use the 1°  
840 basin tilt models from our Series I as an example of early state salt tectonic deformation systems along a  
841 young passive margin, and the 3° basin tilt models to interpret structures in more mature systems.

842

843 Another limitation concerns the lack of syn-kinematic (or post-salt) sedimentation. Syn-kinematic  
844 sedimentation is generally considered to accelerate or even dominate downslope displacements in  
845 salt tectonic systems (e.g. Fort et al 2004b; Peel 2014), although in some cases it might have the  
846 opposite effect and stabilize a salt tectonic system. Such stabilization may occur when  
847 sedimentation is concentrated downslope of the salt basin in question (Warsitzka et al. 2021), or  
848 when such thick overburdens are accumulated sufficiently fast that the instability of the salt units is  
849 not sufficient to cause deformation (Hudec & Jackson 2007). Either way, our models did contain no  
850 syn-kinematic sedimentation and are thus not fully appropriate for interpreting (the more evolved  
851 stages of) sediment-rich salt tectonic systems (Goteti et al. 2013)

852

853 A final limitation is linked to the length of salt basins; as pointed out by Brun & Fort (2008, 2011),  
854 and Tari & Jabour (2013), the length of an evaporite basin has an important influence on its stability  
855 as well. When increasing the width of a salt basin, the necessary degree of margin inclination (angle  
856  $\alpha$ , Fig. 2c) strongly decreases (Brun & Fort 2011). Indeed, small isolated basins are known to only  
857 allow moderate deformation (Tari & Jabour 2013), perhaps illustrated by our experiments as well,  
858 since deformation only occurs above the viscous layer, limiting the system to the extent of salt  
859 basin. Since our models have a constant length of 60 cm, the observed influence of different salt  
860 thicknesses represents only part of the parameter space.

861

862

#### 862 4.5. Comparison with natural examples

863

864 A direct comparison between our generic models and natural examples of salt tectonic systems is  
865 challenging due to various factors. First, the exact initial geometry of salt basins is often debatable,  
866 as the quality of structural reconstructions is affected by the ductile evaporite behavior and the  
867 significant lateral displacements occurring in such systems (e.g. Marton et al. 2000). Furthermore,  
868 salt basin geometries can vary greatly along passive margins (e.g. Marton et al. 2000; PFA 2011;  
869 Guerra and Underhill 2012; Deptuck & Kendell 2017), and initial gravity-gliding structures may be  
870 overprinted by large prograding sedimentary systems that dominate the margins in later stages (e.g.  
871 Peel 2014). Nevertheless, we here present two end member examples that have reasonably well  
872 constrained parameters, (Lower Congo Basin and Scotian Margin, Figs. 15 and 16), which we  
873 compare to our experiments with constant mean salt thickness models and 3° basin tilt.

874

875 The Lower Congo Basin is situated on the Atlantic margin of Angola, which started separating from  
876 its Brazilian conjugate in the Early Cretaceous (e.g. Fairhead & Wilson 2005; Heine et al. 2013, and  
877 references therein). During the final stages of break-up in the Aptian, marine transgression led to  
878 the formation of extensive evaporite deposits in sag basins on both margins (e.g. Davison 2007). In  
879 the Lower Congo Basin, the depocenter of this sag basin was situated rather downslope (Marton et  
880 al. 2000, Fig. 15a). As the margin tilted oceanward, the salt became unstable and formed the  
881 classical salt tectonic domains that we also observe in our models (Spathopoulos 1996; Valle et al.  
882 2001, Fig. 15b). Importantly however, is the fact that sedimentation in these early phases was  
883 broadly distributed (Marton et al. 2000, Fig. 15b, c), which fits the observation that upslope  
884 topography variations are rather gradual in our experiments with downslope depocenters (Fig.13).  
885 Such a bathymetry allowed for widespread sedimentation in the natural example (Fig. 14b, c), until  
886 the influx of large amounts of sediments from the Congo Fan prograded into the system (Fig. 14d)  
887 making further comparisons impractical.

888

889 An example of a salt basin with upslope depocenter is found along the Scotian Margin, at section  
890 NS 2000, offshore Canada (Fig. 16). Here, large Triassic salt units were deposited at the end of the  
891 opening of the Central Atlantic and subsequently tilted (PFA 2011; Biari et al. 2017). As a result,  
892 post-salt units started to move downslope, synchronously creating most accommodation space  
893 higher upslope allowing for the deposition of thicker post-salt units (Fig. 16b), similar to our models.  
894 Also in this case, large-scale sedimentation eventually caught up and started controlling the system  
895 (PFA 2011; Fig. 16d). It may be noted that some authors propose sedimentation to be the main  
896 driving force during the whole salt tectonic evolution of the margin (Albertz & Beaumont 2010;  
897 Albertz et al. 2010), and that considerable variations in salt basin geometry occur along the Scotian  
898 margin (e.g. PFA 2011; Deptuck & Kendell 2017).

899

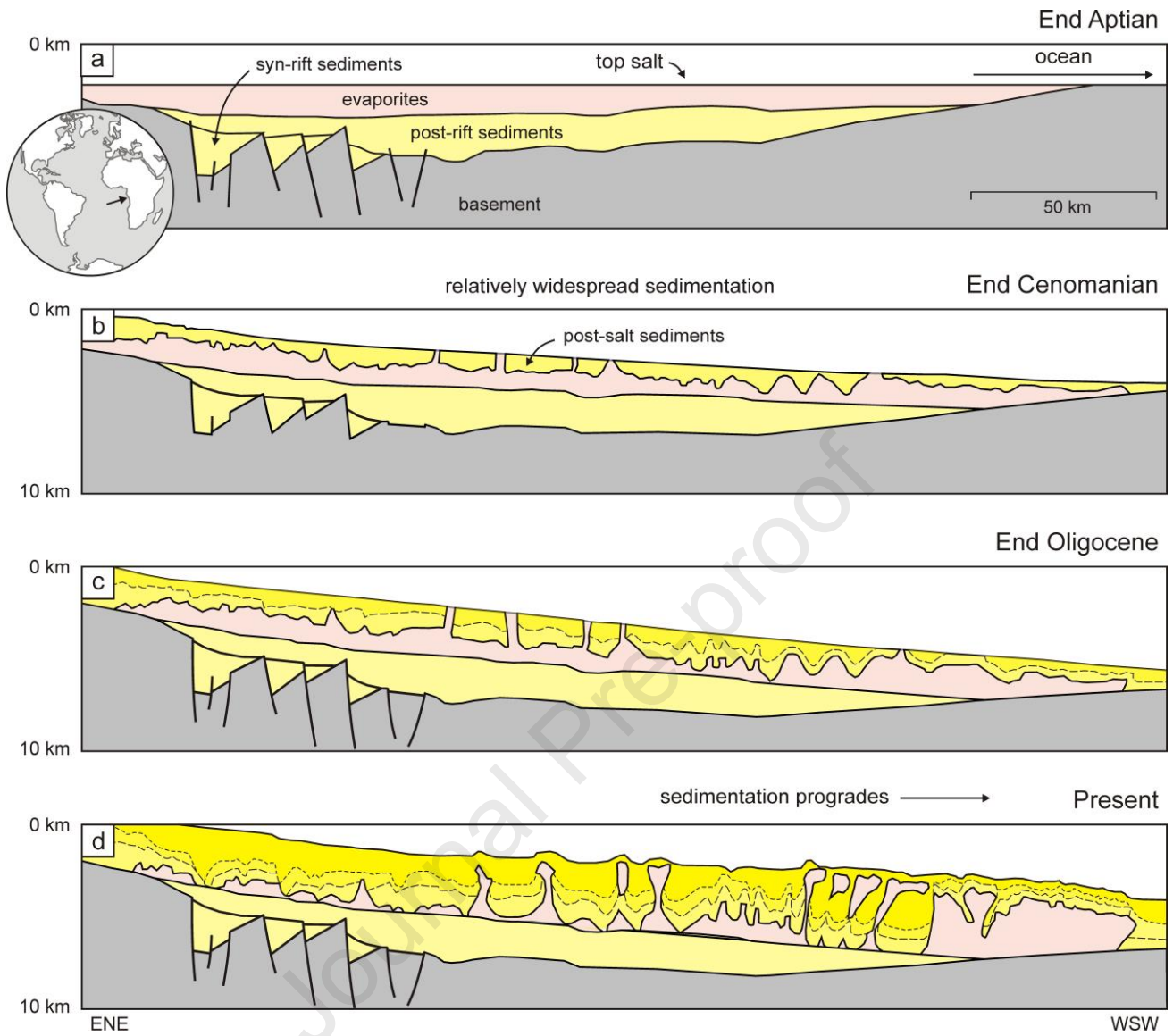
900 Our results fit reasonably well with the presented natural examples; although syn-tectonic  
901 sedimentation is not directly incorporated in our experiments (see section 4.4), we see a fair positive  
902 correlation between post-salt accommodation space generation in model and nature as a function of  
903 salt basin depocenter location (i.e. the loci of thickest, more mobile salt layers). Yet we must  
904 perhaps stress that the dominant mechanism controlling salt tectonics on passive margins (i.e.  
905 dominant spreading due to sedimentary loading vs. dominant gliding due to margin tilt) is still  
906 debated (e.g. Schultz-Ela 2001; Brun & Fort 2011; 2012; Rowan et al. 2012; Goteti et al. 2013; Peel  
907 2014; Warren 2016). However, even if gravity spreading could arguably be the dominant  
908 mechanism in some cases (e.g. in the Santos Basin offshore Brazil, Jackson et al. 2015), we should  
909 still expect a very similar relationship between evaporite depocenters and subsequent  
910 sedimentation patterns; in both scenarios, the salt is evacuated and replaced by post-salt deposits.

911

912

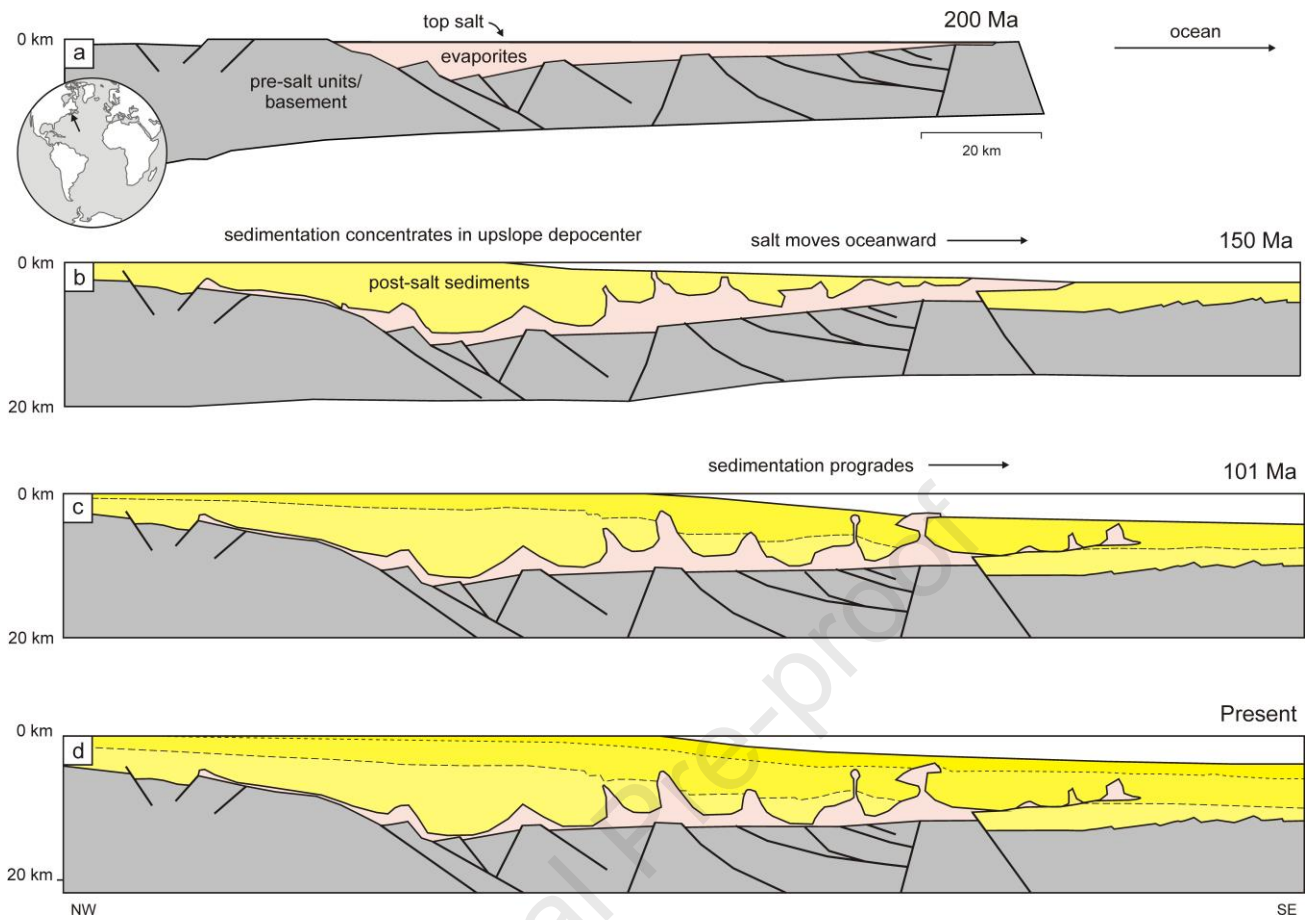
913





914  
915  
916  
917  
918  
919  
920  
921  
922

**Fig. 15.** Evolution of the Lower Congo Basin after evaporite deposition in a basin with a relatively downslope depocenter. Modified after Marton et al. (2000). Dotted lines indicate the top of the sediments from the previous stage(s).



923  
 924  
 925  
 926  
 927  
 928  
 929  
 930  
 931  
 932  
 933  
 934

**Fig. 16.** Evolution of the Scotian Margin (Section NS 2000) after salt deposition in a basin with an upslope depocenter. Modified after PFA (2011). Dotted lines indicate the top of the sediments from the previous stage(s).

## 5. Conclusion

Our analogue modelling efforts to study the effects of evaporite (salt) basin geometry on gravity-gliding style salt tectonics leads us to the following conclusions:

- An assessment of the whole model population shows that first the degree of basin tilt, followed by the mean salt thickness are dominant factors controlling deformation. The more a basin is tilted and the thicker the salt layer, the more deformation occurs. The salt layer thickness itself is partially a result of basin geometry (in combination with the available volume of salt deposits in the system).
- By focusing on a subpopulation of models with constant mean salt thickness and a 3° tilt, we cancel out these effects to isolate the influences of basin geometry, i.e. depocenter location. In these experiments, we find that the location of the salt basin depocenter has various effects on the distribution and expression of tectonic domains in a salt tectonic system (Fig. 13).
- When the depocenter is situated downslope, upslope subsidence is moderate, as the downslope displacement of material is due to the relatively low gravitational potential in the system. Yet the downslope presence of abundant viscous material allows significant localized uplift. The main depocenter being situated farther upslope causes deformation to occur higher upslope as well, concentrating upslope subsidence allowed by the thicker model salt there, while distributing downslope uplift due to the thinner model salt and increased basal drag prevented significant displacements. Also the increased instability due to larger volumes of viscous material sitting higher upslope, means that there is an increase in downslope displacement.
- When comparing our model results with natural examples from Atlantic passive margins, we find a fair correlation expressed in the links between salt depocenter location and subsequent sedimentation patterns. When the salt depocenter is situated upslope, salt evacuation will localize accommodation space generation and post-salt deposition in the upslope part of the system. By contrast, a downslope salt depocenter allows the generation of more distributed accommodation space and sedimentation. These insights should be applied to interpret the early phases of salt tectonic deformation along passive margins, as during later stages, sedimentary loading might become the dominant factor.

## 6. Acknowledgements

We are grateful to the Géosciences, CNRS analog modeling laboratory at Université de Rennes 1, France, (Jean-Jacques Kermarrec and Pascal Roland) for technical support. We warmly thank editor Tiago Alves, and reviewers Tim Dooley and Juan I. Soto for their detailed and constructive feedback that greatly helped to improve the paper. The University of Bern is acknowledged for funding Open Access publication costs, and we are grateful to Kirsten Elger for archiving the supplementary material associated with this paper in the form of a GFZ data publication (Zwaan et al. 2021).

984 **Data availability**

985

986 Supplementary material involving PIV analysis results, digital topography maps and original  
987 measurements are combined in a GFZ data publication (Zwaan et al. 2021), which is publically  
988 accessible here: XXX DOI TO BE FILLED IN XXX.

989

990

991

992

Journal Pre-proof

## Appendix A. Results from models without sand cover (series III)

Next to the models of Series I and II, which included a brittle sand cover to simulate post-salt sediments, we also completed a third series of models without such a brittle cover. All ten of these Series III models (Z1-Z10) involved a 3° basin tilt. Similar to the Series I and II models, we found that the mean model salt thickness has a strong influence on subsequent deformation. Hence we include only the results of the topography and PIV analysis of Models Z1-Z5, highlighting the influence of the model salt basin depocenter, as well as the other characteristics typical of a hypothetical salt tectonic system without post-salt units. The results of the additional models Z6-Z10 can be found in the supplementary materials (Zwaan et al. 2021).

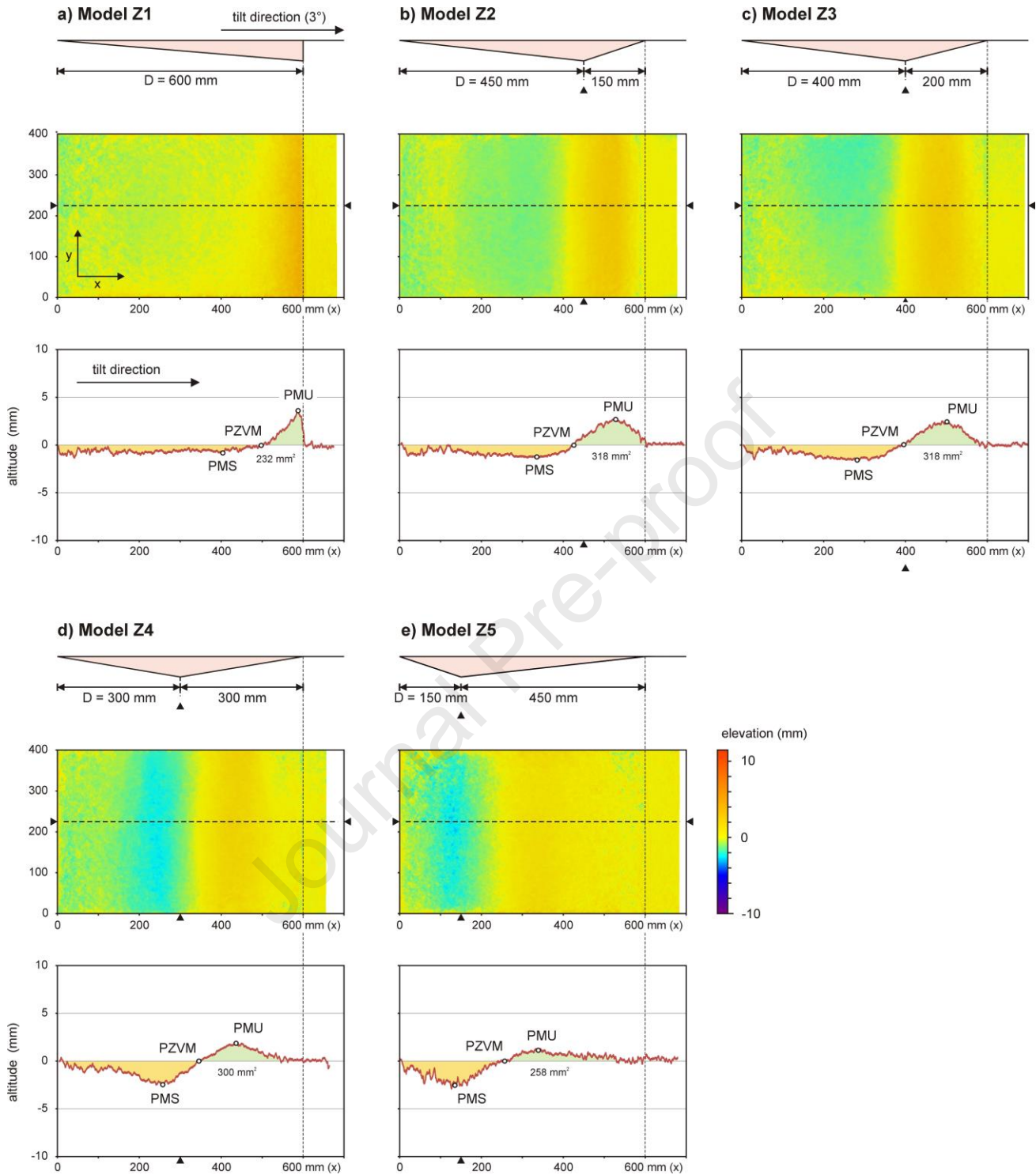
### A1. Topographic analysis results of Models Z1-Z5

The final normalized topography of Models Z1-Z5 is presented in Fig. A1. In contrast to the typical salt tectonic domains found in the Series II models (Figs. 7, 9), Models Z1-Z5 forms a much more gradual relief. This type of topography in the absence of a brittle cover is also reported in the numerical models by Quirk et al. 2012 and Goteti et al. 2013. However, similar to their equivalents Models K-O from Series II, a downslope model salt basin depocenter leads to the PZVM being situated higher upslope, as well as a decrease in maximum downslope uplift and an increase in upslope subsidence (Figs. 7, A1). This is likely for the same reasons as in the Series II models: basal drag preventing downslope motion in basins with relative thin salt layers downslope and ready evacuation of viscous material from upslope salt basin depocenters. A difference with the Series II models is that both the PMU and PMS followed the same trend as the PZVM in Models Z1-Z5, and that the total mass displacement remains rather constant. This is likely because the absence of a brittle layer allows the model salt maximum freedom to adjust to the tilted basin state.

### A2. PIV analysis results of Models Z1-Z5

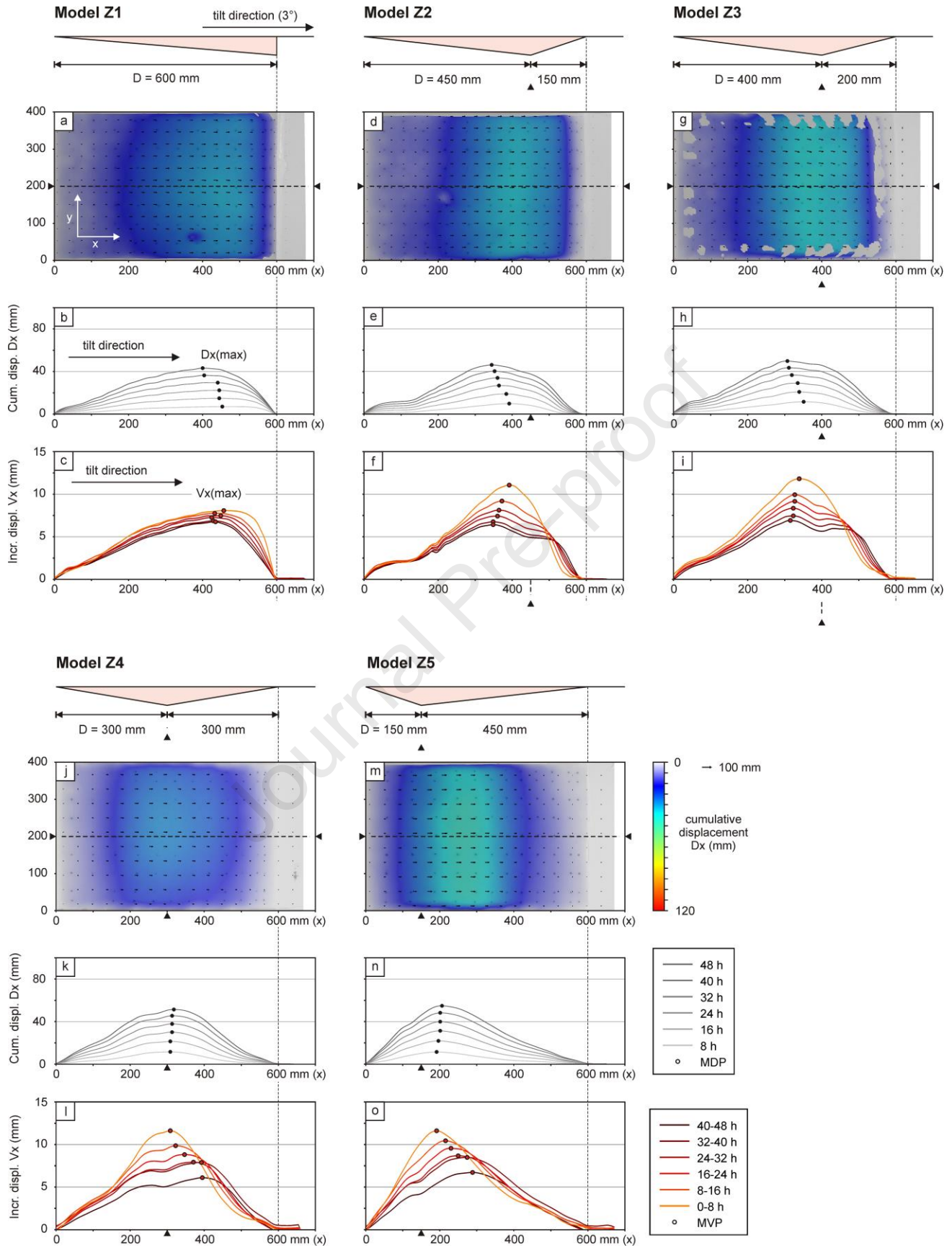
The PIV results of our 3° tilt models Z1-Z5 without sand cover are illustrated in Figs. A2 and A3. Where the equivalent experiments with sand cover developed clear plateau-shaped displacement curves representing the typical salt tectonic domains (Fig. 8), the PIV analysis produced much smoother, almost bell-shaped displacement curves for Models Z1-Z5. These curves represent a distributed extensional domain upslope merging with a distributed downslope compressional domain, and the peak displacement being located in between (Fig. A2). Cumulative displacement (Dxmax) values are slightly lower in equivalent Models K-O from Series II, and increase as the model salt basin depocenter is situated higher upslope (from 45 mm in Model Z1 to 58 mm in Model Z5). This lower maximum cumulative displacement with respect to Models K-O is probably due to the absence of mass in the form of a sand cover accelerating deformation. Another effect of the model salt depocenter location is the evolution of the MVP (Fig. A3). As seen in the model with sand cover in the main text, displacement rates were highest during the initial phases and decreased towards the end of the model run, yet we also found that the MVP either migrated upslope or downslope, depending on the location of the model salt basin depocenter. We speculate that this is related to the bulge-shape of the surface deformation; the MVP might represent the crest of the bulge, which may move downslope fast if material flows out of an upslope salt basin depocenter, or which may be stalled in the opposite situation.





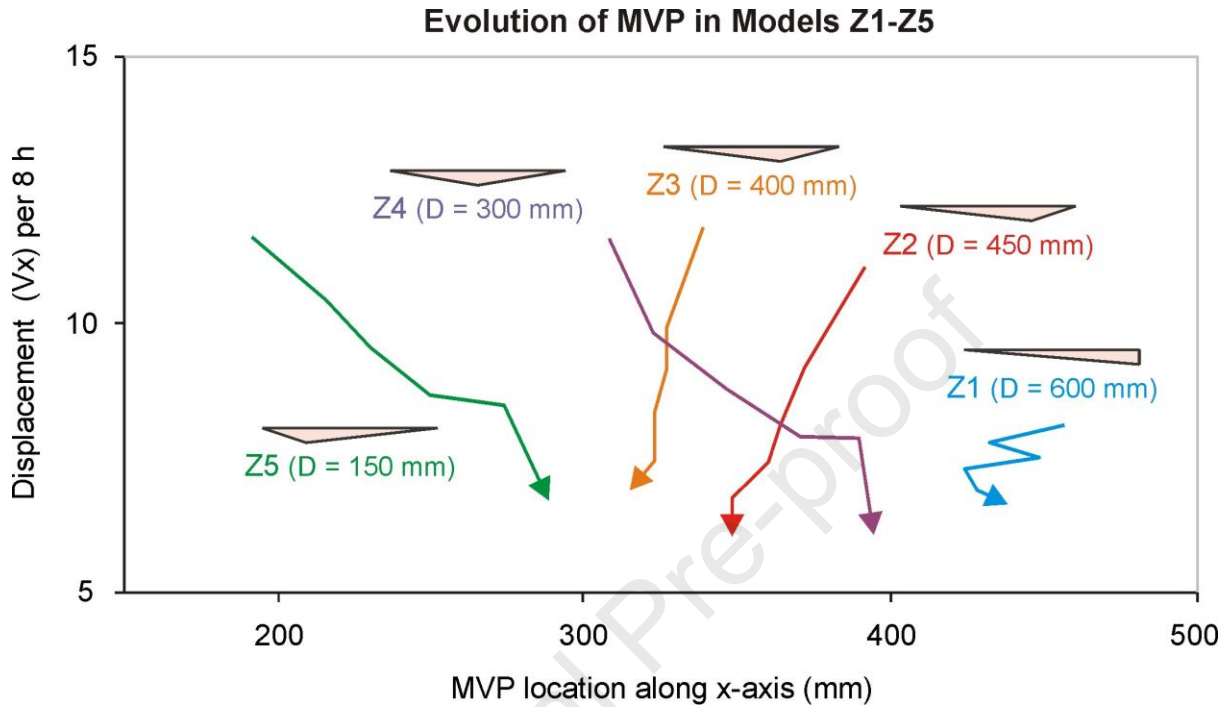
1043  
 1044  
 1045  
 1046  
 1047  
 1048  
 1049  
 1050  
 1051

**Fig. A1.** Final normalized topography of Models Z1-Z5 from Series III ( $3^\circ$  basin tilt, basin shapes 1-5 with constant mean salt thickness, but no sand cover) in map view and along a central section. PZVM: point of zero vertical motion, PMS: point of maximum subsidence, PMU: point of maximum uplift. For more details on definitions, see Fig. 3.



1052  
1053

1054 **Fig. A2.** PIV-derived surface displacements of models Z1-Z5 from Series III ( $3^\circ$  basin tilt, basin  
 1055 shapes 1-5, with constant mean salt thickness), shown in both map view ( $D_x$  only) and plotted on  
 1056 along-axis profiles (both  $D_x$  and  $V_x$ ). MDP: maximum displacement point. MVP: maximum  
 1057 displacement point. For more details on definitions, see Fig. 3.  
 1058  
 1059



1060  
 1061  
 1062 **Fig. A3.** Evolution of the maximum velocity point or MVP (location and associated  $V_{y_{max}}$ ) over time  
 1063 for Models Z1-Z5. The arrows indicate the direction of evolution.  
 1064  
 1065  
 1066  
 1067  
 1068  
 1069  
 1070  
 1071  
 1072

1073 **References**

1074

1075 Adam, J., J.L. Urai, B. Wieneke, O. Oncken, K. Pfeiffer, N. Kukowski, J. Lohrmann, S. Hoth, W. van  
 1076 der Zee, J. Schmatz, (2005), Shear localisation and strain distribution during tectonic faulting - New  
 1077 insights from granular-flow experiments and high-resolution optical image correlation techniques,  
 1078 *Journal of Structural Geology*, 27(2), 183-301.

1079 <http://doi.org/10.1016/j.jsg.2004.08.008>

1080

1081 Adam, J., Krezsek, C. 2012. Basin-scale salt tectonic processes of the Laurentian Basin, Eastern  
 1082 Canada: insights from integrated regional 2-D seismic interpretation and 4D physical experiments.  
 1083 *Geological Society, London, Special Publication*, 363, 331–360. <https://doi.org/10.1144/SP363.15>

1084

1085 Adam, J., Ge., Z., Sanchez, M. 2012. Post-rift salt tectonic evolution and key control factors of the  
 1086 Jequitinhonha deepwater fold belt, central Brazil passive margin: Insights from scaled physical  
 1087 experiments. *Marine and Petroleum Geology* 31, 70-100.

1088 <https://doi.org/10.1016/j.marpetgeo.2012.06.008>

1089

1090 Albertz, M., Beaumont, C. 2010. An investigation of salt tectonic structural styles in the Scotian  
 1091 Basin, offshore Atlantic Canada: 2. Comparison of observations with geometrically complex  
 1092 numerical models. *Tectonics* 27, TC4018. <https://doi.org/10.1029/2009TC002540>

1093

1094 Albertz, M., Beaumont, C., Shimeld, J.W., Ings, S.J., Gradmann, S. 2010. An investigation of salt  
 1095 tectonic structural styles in the Scotian Basin, offshore Atlantic Canada: 1. Comparison of  
 1096 observations with geometrically simple numerical models. *Tectonics* 29, TC4017.

1097 <https://doi.org/10.1029/2009TC002539>

1098

1099 Allen, J., Beaumont, C. 2012. Impact of inconsistent density scaling on physical analogue models of  
 1100 continental margin scale salt tectonics. *Journal of Geophysical Research* 117, B08103.

1101 <https://doi.org/10.1029/2012JB009227>

1102

1103 Allen, J., Beaumont, C. 2015. Continental margin syn-rift salt tectonics at intermediate width  
 1104 margins. *Basin Research*, 28, 598–633. <https://doi.org/10.1111/bre.12123>

1105

1106 Augustin, N., Devey, C.W., van der Zwan, F., Feldens, P., Tominaga, M., Bantan, R.A.,  
 1107 Kwasnischka, T. 2014. The rifting to spreading transition in the Red Sea. *Earth and Planetary  
 1108 Science Letters* 395, 217–230. <http://dx.doi.org/10.1016/j.epsl.2014.03.047>

1109

1110 Biari, Y., Klingelhoefer, F., Sahabi, M., Funck, T., Benabdellouahed, M., Schnabel, M., Reichert, C.,  
 1111 Gutscher, M.-A., Bronner, A., Austin, J.A. 2017. Opening of the central Atlantic Ocean: Implications  
 1112 for geometric rifting and asymmetric initial seafloor spreading after continental breakup. *Tectonics*,  
 1113 36, 1129–1150. <https://doi.org/10.1002/2017TC004596>

1114

1115 Bonatti, E., Emiliani, C., Ostlund, G., Rydell, H. 1971. Final Desiccation of the Afar Rift, Ethiopia.  
 1116 *Science* 172(3982), 468-469. <https://doi.org/10.1126/science.172.3982.468>

1117

1118 Boutelier, D., Schrank, C., Regenauer-Lieb, K. 2019. 2-D finite displacements and strain from  
 1119 particle imaging velocimetry (PIV) analysis of tectonic analogue models with TecPIV. *Solid Earth*  
 1120 10(4), 1123-1139. <https://doi.org/10.5194/se-10-1123-2019>

1121

1122 Brun, J.-P. 1999. Narrow rifts versus wide rifts: inferences for the mechanics of rifting from  
 1123 laboratory experiments. *Philosophical Transactions of the Royal Society London A* 357, 695-712.

1124 <https://doi.org/10.1098/rsta.1999.0349>



- 1125  
 1126 Brun, J.-P., Fort, X. 2004. Compressional salt tectonics (Angolan margin), *Tectonophysics* 382,  
 1127 129–150. <https://doi.org/10.1016/j.tecto.2003.11.014>  
 1128  
 1129 Brun, J.-P., Fort, X. 2008. Entre sel et terre. Structures et mécanismes de la tectonique salifère.  
 1130 Collection Interactions, Vuibert, Paris.  
 1131 <https://hal-insu.archives-ouvertes.fr/insu-00334744>  
 1132  
 1133 Brun, J.-P., Fort, X. 2011. Salt tectonics at passive margins: Geology versus models. *Marine and*  
 1134 *Petroleum Geology* 28, 1123–1145, <https://doi.org/10.1016/j.marpetgeo.2011.03.004>  
 1135  
 1136 Brun, J.-P., Fort, X. 2012. Salt tectonics at passive margins: Geology versus models – Reply.  
 1137 *Marine and Petroleum Geology* 37, 195-208. <https://doi.org/10.1016/j.marpetgeo.2012.04.008>  
 1138  
 1139 Cobbold, P.R., Szatmari, P., 1991. Radial gravitational gliding on passive margins. *Tectonophysics*  
 1140 188, 249-289. [https://doi.org/10.1016/0040-1951\(91\)90459-6](https://doi.org/10.1016/0040-1951(91)90459-6)  
 1141  
 1142 Cobbold, P., Rosello, E., Vendeville, B., 1989. Some experiments on interacting sedimentation and  
 1143 deformation above salt horizons. *Bulletin de la Société Géologique de France* 1989, 3, 453–460.  
 1144 <https://doi.org/10.2113/gssgfbull.V.3.453>  
 1145  
 1146 Davison, I. 2007. Geology and tectonics of the South Atlantic Brazilian  
 1147 In: Ries, A.C., Butler, R.W.H., Graham, R.H. (Eds). *Deformation of the Continental Crust: The*  
 1148 *Legacy of Mike Coward*. Geological Society, London, Special Publications 272, 345-359.  
 1149 <http://dx.doi.org/10.1144/GSL.SP.2007.272.01.18>  
 1150  
 1151 Davison, I., Anderson, L., Nutall, P. 2012. Salt deposition, loading and gravity drainage in the  
 1152 Campos and Santos salt basins. In: Alsop, G.I., Archer, S.G., Hartley, A.J., Grant, N.T.,  
 1153 Hodgkinson, R. (Eds.) *Salt Tectonics, Sediments and Prospectivity*. Geological Society, London,  
 1154 Special Publications 363, 159 – 173. <http://dx.doi.org/10.1144/SP363.8>  
 1155  
 1156 Demercian, S., Szatmari, P., Cobbold, P.R. 1993. Style and pattern of salt diapirs due to thin-  
 1157 skinned gravitational gliding, Campos and Santos basins, offshore Brazil. *Tectonophysics* 3-4, 393-  
 1158 433. [https://doi.org/10.1016/0040-1951\(93\)90351-J](https://doi.org/10.1016/0040-1951(93)90351-J)  
 1159  
 1160 Deptuck, M.E., Kendell, K.L., 2017. A Review of Mesozoic-Cenozoic Salt Tectonics Along the  
 1161 Scotian Margin, Eastern Canada. In: Soto, J.I., Flinch, J.F., Tari, G. (Eds). *Permo-Triassic Salt*  
 1162 *Provinces of Europe, North Africa and the Atlantic Margins*, Elsevier, 287-312.  
 1163 <https://doi.org/10.1016/B978-0-12-809417-4.00014-8>  
 1164  
 1165 Dooley, T.P., Hudec, M.R. 2017. The effects of base-salt relief on salt flow and suprasalt  
 1166 deformation patterns — Part 2: Application to the eastern Gulf of Mexico. *Interpretation* 5(1), SD25–  
 1167 SD38. <http://dx.doi.org/10.1190/INT-2016-0088.1>  
 1168  
 1169 Dooley, T.P., Hudec, M.R., Carruthers, D., Jackson, M.P.A., Luo, G. 2017. The effects of base-salt  
 1170 relief on salt flow and suprasalt deformation patterns — Part 1: Flow across simple steps in the base  
 1171 of salt. *Interpretation* 5(1), SD1–SD23. <https://doi.org/10.1190/INT-2016-0087.1>  
 1172  
 1173 Dooley, T.P., Hudec, M.R., Pichel, L.M., Jackson, M.P.A. 2018. The impact of base-salt relief on salt  
 1174 flow and suprasalt deformation patterns at the autochthonous, paraautochthonous and  
 1175 allochthonous level: insights from physical models. In: McClay, K.R., Hammerstein, J.A. (eds).



- 1176 Passive Margins: Tectonics, Sedimentation and Magmatism. Geological Society, London, Special  
1177 Publications 476. <https://doi.org/10.1144/SP476.13>  
1178
- 1179 Fairhead, J.D., Wilson, M., 2005, Plate tectonic processes in the South Atlantic Ocean: Do we need  
1180 deep mantle plumes? In: Foulger, G.R., Natland, J.H., Presnall, D.C., Anderson, D.L., (Eds). Plates,  
1181 plumes, and paradigms: Geological Society of America Special Paper 388, 537–553.  
1182 [https://doi.org/10.1130/2005.2388\(32\)](https://doi.org/10.1130/2005.2388(32))  
1183
- 1184 Ferrer, O., Gratacós, O., Roca, E., Muñoz, J.A. 2017. Modeling the interaction between presalt  
1185 seamounts and gravitational failure in salt-bearing passive margins: The Messinian case in the  
1186 northwestern Mediterranean Basin. *Interpretation* 5(1), SD99–SD117.  
1187 <https://doi.org/10.1190/INT-2016-0096.1>  
1188
- 1189 Fort, X., Brun, J.-P., Chauvel, F. 2004a. Salt tectonics on the Angolan margin, synsedimentary  
1190 deformation processes. *AAPG Bulletin* 88(11) 1523-1544. <https://doi.org/10.1306/06010403012>  
1191
- 1192 Fort, X., Brun, J.-P., Chauvel, F. 2004b. Contraction induced by block rotation above salt (Angolan  
1193 margin). *Marine and Petroleum Geology* 21, 1281-1294.  
1194 <https://doi.org/10.1016/j.marpetgeo.2004.09.006>  
1195
- 1196 Gamboa L.A.P., Machado M.A.P., da Silveira D.P., de Freitas J.T.R., da Silva S.R.P., 2008.  
1197 Evaporitos estratificados no Atlântico Sul, in: W.U. Mohriak, W.U., Szatmariand P., Couto Anjos,  
1198 S.M (eds.), *Sal: Geologia e Tectônica*, Edições Beca, Petrobras, Sao Paulo, 340- 359.  
1199
- 1200 Garcia, S.F.M., Letouzey, J., Rudkiewicz, J.-L., Filho, A.D., Frizon de Lamotte, D.F. 2012. Structural  
1201 modeling based on sequential restoration of gravitational salt deformation in the Santos Basin  
1202 (Brazil). *Marine and Petroleum Geology* 35, 337-353.  
1203 <https://doi.org/10.1016/j.marpetgeo.2012.02.009>  
1204
- 1205 Gaullier, V., Brun, J.-P., Guérin, G., Lecanu, H. 1993. Raft tectonics: the effects of residual  
1206 topography below a salt décollement. *Tectonophysics* 228, 363-381.  
1207 [https://doi.org/10.1016/0040-1951\(93\)90349-O](https://doi.org/10.1016/0040-1951(93)90349-O)  
1208
- 1209 Gaullier, V., Vendeville, B.C., 2005. Salt tectonics driven by sediment progradation. Part II: Radial  
1210 spreading of sedimentary lobes prograding above salt. *American Association of Petroleum*  
1211 *Geologists Bulletin* 89, 1081-1089.  
1212 <https://doi.org/10.1306/03310503064>  
1213
- 1214 Ge, Z., Rosenau, M., Warsitzka, M., Gawthorpe, R.L. 2019a. Overprinting translational domains in  
1215 passive margin salt basins: insights from analogue modelling. *Solid Earth* 10, 1283-1300.  
1216 <https://doi.org/10.5194/se-10-1283-2019>  
1217
- 1218 Ge, Z., Warsitzka, M., Rosenau, M., Gawthorpe, R.L. 2019b. Progressive tilting of salt-bearing  
1219 continental margins controls thin-skinned deformation. *Geology* 47, 1122-1126.  
1220 <https://doi.org/10.1130/G46485.1>  
1221
- 1222 Gemmer, L., Ings, S.J., Medvedev, G., Baumont, C. 2004. Salt tectonics driven by differential  
1223 sediment loading: stability analysis and finite-element experiments.  
1224
- 1225 Gemmer, L., Baumont, C., Ings, S. J. 2005. Dynamic modelling of passive margin salt tectonics:  
1226 effects of water loading, sediment properties and sedimentation patterns. *Basin Research* 17, 383–  
1227 402. <https://doi.org/10.1111/j.1365-2117.2005.00274.x>

- 1228  
 1229 Goteti, R., Beaumont, C., Ings, S.J. 2013. Factors controlling early stage salt tectonics at rifted  
 1230 continental margins and their thermal consequences. *Journal of Geophysical Research: Solid Earth*  
 1231 118, 3190-3220. <https://doi.org/10.1002/jgrb.50201>  
 1232
- 1233 Guerra, M.C.M., Underhill, J.R. 2012. Role of halokinesis in controlling structural styles and  
 1234 sediment dispersal in the Santos Basin, offshore Brazil. In: Alsop, G.I., Archer, S.G., Hartley, A.J.,  
 1235 Grant, N.T., Hodgkinson, R. (Eds). *Salt Tectonics, Sediments and Prospectivity*. Geological Society,  
 1236 London, Special Publications 363, 175-206.  
 1237 <http://dx.doi.org/10.1144/SP363.9>  
 1238
- 1239 Heine, C. Zoethout, J.M., Müller, R.D. 2013. Kinematics of the South Atlantic rift . *Solid Earth* 4,  
 1240 215-253. <https://doi.org/10.5194/se-4-215-2013>  
 1241
- 1242 Hubbert, M. K. 1937. Theory of scaled models as applied to the study of geological structures, *Geol.*  
 1243 *Soc. Am. Bull.*, 48, 1459–1520. <https://doi.org/10.1130/GSAB-48-1459>  
 1244
- 1245 Hudec, M.R., Jackson, P.A. 2004. Regional restoration across the Kwanza Basin, Angola: Salt  
 1246 tectonics triggered by repeated uplift of a metastable passive margin. *AAPG Bulletin* 88, 971-990.  
 1247 <https://doi.org/10.1306/02050403061>  
 1248
- 1249 Hudec, M.R., Jackson, M.P.A. 2006. Advance of allochthonous salt sheets in passive margins and  
 1250 orogens. *AAPG Bulletin* 90 1535–1564. <https://doi.org/10.1306/05080605143>  
 1251 [https://pubs.geoscienceworld.org/aapgbull/article-abstract/88/7/971/40169/Regional-restoration-](https://pubs.geoscienceworld.org/aapgbull/article-abstract/88/7/971/40169/Regional-restoration-across-the-Kwanza-Basin?redirectedFrom=fulltext)  
 1252 [across-the-Kwanza-Basin?redirectedFrom=fulltext](https://pubs.geoscienceworld.org/aapgbull/article-abstract/88/7/971/40169/Regional-restoration-across-the-Kwanza-Basin?redirectedFrom=fulltext)  
 1253
- 1254 Hudec, M.R, Jackson, M.P.A., 2007. Terra infirma: Understanding salt tectonics, *Earth-Science*  
 1255 *Reviews* 82, 1-28. <https://doi.org/10.1016/j.earscirev.2007.01.001>  
 1256
- 1257 Hudec, M.R., Jackson, M.P.A. 2012. De Re Salica: Fundamental principles of salt tectonics. In:  
 1258 Roberts, D.G., Bally, A.W. (Eds.). *Regional Geology and Tectonics: Phanerozoic Passive Margins,*  
 1259 *Cratonic Basins and Global Tectonic Maps*, Elsevier, 18-41. [https://doi.org/10.1016/B978-0-444-](https://doi.org/10.1016/B978-0-444-56357-6.00001-9)  
 1260 [56357-6.00001-9](https://doi.org/10.1016/B978-0-444-56357-6.00001-9)  
 1261
- 1262 Ings, S., Beaumont, C., Gemmer, L., 2004. Numerical modeling of salt tectonics on passive  
 1263 continental margins: preliminary assessment of the effects of sediment loading, buoyancy, margin  
 1264 tilt, and isostasy. In: Post, P.J., Olson, D.L., Lyons, K.T., Palmes, S.L., Harrison, P.F., Rosen, N.C.  
 1265 (Eds.), *Salt Sediment Interactions and Hydrocarbon Prospectivity: 24th Annual GCSSEPM*  
 1266 *Foundation Bob F. Perkins Research Conference Proceedings*, 36-68.  
 1267 <https://doi.org/10.5724/qcs.04.24.0036>  
 1268
- 1269 Jackson, M.P.A., Talbot 1986. External shapes, strain rates, and dynamics of salt structures. *GSA*  
 1270 *Bulletin* 97, 305–323. [https://doi.org/10.1130/0016-7606\(1986\)97<305:ESSRAD>2.0.CO;2](https://doi.org/10.1130/0016-7606(1986)97<305:ESSRAD>2.0.CO;2)  
 1271
- 1272 Jackson, M.P.A., Hudec, M.R., 2017. *Salt Tectonics: Principles and Practice*. Cambridge University  
 1273 Press. <https://doi.org/10.1017/9781139003988>  
 1274
- 1275
- 1276 Jackson, C.A.-L., Jackson, M.P.A., Hudec. M.R. 2015. Understanding the kinematics of salt-bearing  
 1277 passive margins: A critical test of competing hypotheses for the origin of the Albian Gap, Santos  
 1278 Basin, offshore Brazil. *GSA Bulletin* 127, 1170-1751. <https://doi.org/10.1130/B31290.1>  
 1279

- 1280 Loncke, L., Vendeville, B.C., Gaullier, V., Mascle, J. 2010. Respective contributions of tectonic and  
 1281 gravity-driven processes on the structural pattern in the Eastern Nile deep-sea fan: insights from  
 1282 physical experiments. *Basin Research* 22, 765-782.  
 1283 <https://doi.org/10.1111/j.1365-2117.2009.00436.x>  
 1284
- 1285 Maillard, A., Gaullier, V., Vendeville, B.C., Odonne, F. 2003. Influence of differential compaction  
 1286 above basement steps on salt tectonics in the Ligurian-Provençal Basin, northwest Mediterranean.  
 1287 *Marine and Petroleum Geology* 20, 13-27.  
 1288 [https://doi.org/10.1016/S0264-8172\(03\)00022-9](https://doi.org/10.1016/S0264-8172(03)00022-9)  
 1289
- 1290 Marton, L.G., Tari, G.C., Lehmann, C.T. 2000. Evolution of the Angolan passive margin, West  
 1291 Africa, with emphasis on post-salt structural styles. *AGU Geophysical Monographs Series* 115, 129-  
 1292 149. <https://doi.org/10.1029/GM115p0129>  
 1293
- 1294 Mauduit, T., Guerin, G., Brun, J.-P., Lecanu, H., 1997. Raft tectonics: the effects of basal slope  
 1295 angle and sedimentation rate on progressive extension. *Journal of Structural Geology*, 19, 1219-  
 1296 1230. [https://doi.org/10.1016/S0191-8141\(97\)00037-0](https://doi.org/10.1016/S0191-8141(97)00037-0)  
 1297
- 1298 Mauduit, T., Brun, J.-P., 1998. Growth fault/rollover systems: birth, growth, and decay. *Journal of*  
 1299 *Geophysical Research* 103, 119-136. <https://doi.org/10.1029/97JB02484>  
 1300
- 1301 McClay, K.R., Dooley, T., Whitehouse, P., Mills, M. 2002. 4-D evolution of rift systems: Insights from  
 1302 scaled physical models. *AAPG Bulletin*, 86, 935–959.  
 1303
- 1304 Modica, C.J., Brush, E.R. 2004. Postrift sequence stratigraphy, paleogeography, and fill history of  
 1305 the deep-water Santos Basin, offshore southeast Brazil. *AAPG Bulletin* 88, 923-945.  
 1306 <https://doi.org/10.1306/01220403043>  
 1307
- 1308 Peel, F.J., Travis, C.J., Hossack, J.R., 1995. Genetic Structural Provinces and Salt Tectonics of the  
 1309 Cenozoic Offshore U.S. Gulf of Mexico: A Preliminary Analysis. In: Jackson, M.P.A., Roberts, D.G.,  
 1310 Snelson, S. (eds) *Salt Tectonics: A Global Perspective*. *AAPG Memoir* 65, 153-175.  
 1311 <https://doi.org/10.1306/M65604C7>  
 1312 <http://archives.datapages.com/data/specpubs/memoir65/ch07/0153.htm>  
 1313
- 1314 Peel, F.J. 2014. How do salt withdrawal minibasins form? Insights from forward modelling, and  
 1315 implications for hydrocarbon migration. *Tectonophysics* 630, 222–235  
 1316 <http://dx.doi.org/10.1016/j.tecto.2014.05.027>  
 1317
- 1318 PFA (Nova Scotia Play Fairway Analysis Atlas) 2011. Nova Scotia Department of Energy and  
 1319 Mines, Canada. <https://energy.novascotia.ca/oil-and-gas/offshore/play-fairway-analysis/analysis>  
 1320
- 1321 Pichel, L.M., Peel, F., Jackson, C.A.-L., Huuse, M. 2018. Geometry and kinematics of salt-detached  
 1322 ramp syncline basins. *Journal of Structural Geology* 115, 208-230.  
 1323 <https://doi.org/10.1016/j.jsq.2018.07.016>  
 1324
- 1325 Pichel, L.M., Finch, E., Gawthorpe, R.L. 2019. The impact of pre - salt rift topography on salt  
 1326 tectonics: A discrete - element modeling approach. *Tectonics*, 38.  
 1327 <https://doi.org/10.1029/2018TC005174>  
 1328
- 1329 Quirk, D.G., Schødt, N., Lassen, B., Ings, S.J., Hsu, D., Hirsch, K.K., Von Nicolai, C. 2012. Salt  
 1330 tectonics on passive margins: examples from Santos, Campos and Kwanza basins. In: Alsop, G.I.,  
 1331 Archer, S.G., Hartley, A.J., Grant, N.T., Hodgkinson, R. (eds). *Salt Tectonics, Sediments and*

- 1332 Prospectivity. Geological Society, London, Special Publications 363, 207-244.  
 1333 <https://doi.org/10.1144/SP363.10>  
 1334
- 1335 Ramberg, H. 1981. Gravity, Deformation and the Earth's Crust: In Theory, Experiments and  
 1336 Geological Application. Academic Press, London.  
 1337
- 1338 Ritter, M. C., Rosenau, M., Oncken, O. 2018. Growing faults in the lab: Insights into the scale  
 1339 dependence of the fault zone evolution process. *Tectonics*, 37.  
 1340 <https://doi.org/10.1002/2017TC004787>  
 1341
- 1342 Rowan M.G., Peel, F.J., Vendeville, B.C. 2004. Gravity-driven Fold Belts on Passive Margins. In:  
 1343 McClay, K.R. (ed) Thrust Tectonics and Hydrocarbon Systems. AAPG Memoir 82, 157-182.  
 1344 <https://doi.org/10.1306/M82813C9>  
 1345
- 1346 Rowan, M.G. 2014. Passive-margin salt basins: hyperextension, evaporite deposition, and salt  
 1347 tectonics. *Basin Research* 26, 154-182. <https://doi.org/10.1111/bre.12043>  
 1348
- 1349 Rowan, M.G., 2018. The South Atlantic and Gulf of Mexico salt basins: crustal thinning, subsidence  
 1350 and accommodation for salt and presalt strata. In: McClay, K.R., Hammerstein, J.A. (Eds.). *Passive*  
 1351 *Margins: Tectonics, Sedimentation and Magmatism*. Geological Society, London, Special  
 1352 Publications 476, 333-363. <https://doi.org/10.1144/SP476.6>  
 1353
- 1354 Rowan, M.G., Peel, F.J., Vendeville, B.C., Gaullier, V. 2012. Salt tectonics at passive margins:  
 1355 Geology versus models – Discussion. *Marine and Petroleum Geology* 37, 184-194.  
 1356 <https://doi.org/10.1016/j.marpetgeo.2012.04.007>  
 1357
- 1358 Rudolf, M., Boutelier, D., Rosenau, M., Schreurs, G., Oncken, O., 2016. Rheological benchmark of  
 1359 silicone oils used for analog modeling of short- and long-term lithospheric deformation,  
 1360 *Tectonophysics* 684, 12-22. <http://dx.doi.org/10.1016/j.tecto.2015.11.028>  
 1361
- 1362 Schultz-Ela, D.D., 2001. Excursus on gravity gliding and gravity spreading. *Journal of Structural*  
 1363 *Geology* 23, 725-731. [https://doi.org/10.1016/S0191-8141\(01\)00004-9](https://doi.org/10.1016/S0191-8141(01)00004-9)  
 1364
- 1365 Spathoplous, F. 1996. An insight on salt tectonics in the Angola Basin, South Atlantic. In: Alsop,  
 1366 G.I., Blundell, D.J., Davison, I. (Eds) *Salt tectonics*. Geological Society, London, Special Publication  
 1367 11, 153-174. <https://doi.org/10.1144/GSL.SP.1996.100.01.11>  
 1368
- 1369 Strozyk, F., Back, S., Kukla, P.A. 2017. Comparison of the rift and post-rift architecture of  
 1370 conjugated salt and salt-free basins offshore Brazil and Angola/Namibia, South Atlantic.  
 1371 *Tectonophysics* 716, 204-224. <http://dx.doi.org/10.1016/j.tecto.2016.12.012>  
 1372
- 1373 Tari, G., Jabour, H. 2013. Salt tectonics along the Atlantic margin of Morocco. In: Mohriak, W.U.,  
 1374 Danforth, A., Post, P.J., Brown, D.E., Tari, G.C., Nemčok, M., Sinha, S.T. (Eds.) *Conjugate*  
 1375 *Divergent Margins*. Geological Society, London, Special Publications 369, 337-353.  
 1376 <http://dx.doi.org/10.1144/SP369.23>  
 1377
- 1378 Valle, P.J., Gjelberg, J.G., Helland-Hansen, W. 2001. Tectonostratigraphic development in the  
 1379 eastern Lower Congo Basin, offshore Angola, West Africa. *Marine and Petroleum Geology* 18, 909-  
 1380 927. [https://doi.org/10.1016/S0264-8172\(01\)00036-8](https://doi.org/10.1016/S0264-8172(01)00036-8)  
 1381
- 1382 Vendeville, B., Cobbold, P.R., Davy, P., Brun, J.P., Chourkoune, P. 1987. Physical models of  
 1383 extensional tectonics at various scales. In: Coward, M.P., Dewey, J.F., Hancock, P.L. (eds.)

- 1384 Continental extension tectonics, Geological Society, London, Special Publications 28, 95-107.  
1385 <https://doi.org/10.1144/GSL.SP.1987.028.01.08>  
1386 Vendeville, B.C., Ge, H., Jackson, M.P.A. 1995. Scale models of salt tectonics during basement-  
1387 involved extension. *Petroleum Geoscience* 1, 179–183. <https://doi.org/10.1144/petgeo.1.2.179>  
1388  
1389 Warren, J.K. 2016. Flowing Salt: Halokinesis. In: *Evaporites: A Geological Compendium* Springer,  
1390 Cham. 491-612. [https://doi.org/10.1007/978-3-319-13512-0\\_6](https://doi.org/10.1007/978-3-319-13512-0_6)  
1391  
1392 Warzitska, M, Závada, P., Jähne-Klingberg, F., Krzywiec, P., 2021. Contribution of gravity gliding in  
1393 salt-bearing rift basins – A new experimental setup for simulating salt tectonics under the influence  
1394 of sub-salt extension and tilting *Solid Earth Discussions* (Preprint) [https://doi.org/10.5194/se-2021-](https://doi.org/10.5194/se-2021-17)  
1395 [17](https://doi.org/10.5194/se-2021-17)  
1396  
1397 Weijermars, R. 1986. Flow behaviour and physical chemistry of bouncing putties and related  
1398 polymers in view of tectonic laboratory applications, *Tectonophysics* 124, 325–358.  
1399 [https://doi.org/10.1016/0040-1951\(86\)90208-8](https://doi.org/10.1016/0040-1951(86)90208-8)  
1400  
1401 Zalán, P.V., Severino, M.C.G., Rigoti, C.A., Magnavita, L.P., Oliveira, J.A.B., Vianna, A.R. 2011. An  
1402 entirely new 3-D view of the crustal and mantle structure of a South Atlantic passive margin –  
1403 Santos, Campos and Espírito Santo Basins, Brazil. *AAPG Search and Discovery Article #30177*.  
1404 [http://www.searchanddiscovery.com/pdfz/documents/2011/30177zalan/ndx\\_zalan.pdf.html](http://www.searchanddiscovery.com/pdfz/documents/2011/30177zalan/ndx_zalan.pdf.html)  
1405 [http://www.searchanddiscovery.com/documents/2011/30177zalan/ndx\\_zalan.pdf](http://www.searchanddiscovery.com/documents/2011/30177zalan/ndx_zalan.pdf)  
1406  
1407 Zwaan, F., Schreurs, G., Naliboff, J., Buitert, S.J.H., 2016. Insights into the effects of oblique  
1408 extension on continental rift interaction from 3D analogue and numerical models. *Tectonophysics*  
1409 693, 239-260. <http://dx.doi.org/10.1016/j.tecto.2016.02.036>  
1410  
1411 Zwaan, F., Schreurs, G., Ritter, M., Santimano, T., Rosenau, M. 2018. Rheology of PDMS-  
1412 corundum sand mixtures from the Tectonic Modelling Lab of the University of Bern (CH), V. 1. GFZ  
1413 Data Services, <https://doi.org/10.5880/figgeo.2018.023>  
1414  
1415 Zwaan, F., Scheurs, G., Buitert, S.J.H. 2019. A systematic comparison of experimental set-ups for  
1416 modelling extensional tectonics. *Solid Earth* 10, 1063-1097.  
1417 <https://doi.org/10.5194/se-10-1063-2019>  
1418  
1419 Zwaan, F., Rosenau, M., Maestrelli, D. (2021). Digital image correlation and topography data from  
1420 analogue modelling experiments addressing the influence of basin geometry on gravity-driven salt  
1421 tectonics at the Tectonic Modelling Lab of the University of Rennes (F).  
1422



## Highlights WAM modelling paper for MPG

(max 5 bullet points, max 2 lines per bullet point)

- We use analogue models to test the effects of salt basin geometry (salt basin depocenter location and mean salt basin thickness) on gravity-style salt tectonics.
- Higher mean salt thickness in a salt basin, and higher degrees of margin tilt increase instability in salt tectonic systems, promoting deformation by gravity gliding
- Salt depocenters situated higher upslope lead to increased subsidence in the upslope part of the margin, faster downslope displacement of material, and a broader uplift zone downslope.
- The location of salt basin depocenters can strongly affect the distribution of newly generated accommodation space available for the deposition of post-salt units
- Our quantitative results may serve to interpret deformation during early-stage salt tectonics, before the effects of synkinematic sedimentation can become dominant

**Declaration of interests**

The authors declare that they have no known competing financial interests or personal relationships that could have appeared to influence the work reported in this paper.

The authors declare the following financial interests/personal relationships which may be considered as potential competing interests:

Journal Pre-proof